

The Fundamental Patterns of Sea Surface Temperature

J. Xavier Prochaska, Erdong Guo, Peter C. Cornillon, Christian E. Buckingham

Abstract—For over 40 years, remote sensing observations of the Earth’s oceans have yielded global measurements of sea surface temperature (SST). With a resolution of approximately 1 km, these data trace physical processes like western boundary currents, cool upwelling at eastern boundary currents, and the formation of mesoscale and sub-mesoscale eddies. To discover the fundamental patterns of SST on scales smaller than 10 km, we developed an unsupervised, deep contrastive learning model named NENYA. We trained NENYA on a subset of 8 million cloud-free cutout images ($\sim 80 \times 80 \text{ km}^2$) from the MODerate-resolution Imaging Spectroradiometer (MODIS) sensor, with image augmentations to impose invariance to rotation, reflection, and translation. The 256-dimension latent space of NENYA defines a vocabulary to describe the complexity of SST and associates images with like patterns and features. We used a dimensionality reduction algorithm to explore cutouts with a temperature interval of $\Delta T = 0.5 - 1 \text{ K}$, identifying a diverse set of patterns with temperature variance on a wide range of scales. We then demonstrated that SST data with large-scale features arise preferentially in the Pacific and Atlantic Equatorial Cold Tongues and exhibit a strong seasonal variation, while data with predominantly sub-mesoscale structure preferentially manifest in western boundary currents, select regions with strong upwelling, and along the Antarctic Circumpolar Current. We provide a web-based user interface to facilitate the geographical and temporal exploration of the full MODIS dataset. Future efforts will link specific SST patterns to select dynamics (e.g., frontogenesis) to examine their distribution in time and space on the globe.

Index Terms—IEEEtran, journal, LATEX, paper, template.

I. INTRODUCTION

DECADES of infrared (IR) observations made from satellite-borne sensors have been used to generate twice-daily (clouds permitting), global sea surface temperature (SST) fields. While dependent upon the specific satellite sensor examined, as well as the level of processing applied, IR measurements nominally have spatial resolutions of 1 km and temperature resolutions of several tenths Kelvin. Moreover, the swath widths of these sensors typically range from 1000 to 2500 km, permitting resolution of both mesoscale (horizontal scales of 30-200 km) and sub-mesoscale ocean phenomena

(horizontal scales of 1-50 km)¹. One notes the two length-scales overlap, in part because of the varying radius of deformation with latitude leading to different ranges for each throughout the literature. Examples of mesoscale phenomena include strong western boundary current systems such as the Gulf Stream, Kuroshio, and Aghulhas Currents, upwelling systems along eastern boundaries such as the California and Benguela Current Systems, tropical instability waves, large-scale eddies and/or baroclinic Rossby waves. Examples of sub-mesoscale processes include finer-scale fronts, filaments, and eddies that often result from stirring and straining by the mesoscale currents, and consequent instabilities that take place at these locations [1], [2]. In summary, IR satellite-derived measurements yield powerful datasets for exploring the physical properties and processes of our ocean over a broad range of spatial and temporal scales.

Impressively, one notes that data from even a single sensor, such as the MODerate-resolution Imaging Spectroradiometer (MODIS) dataset, satisfies most characteristics of so-called “big data.” For example, the Level-2 (L2) SST archive of the processed Aqua MODIS data stream (2003-2021, inclusive) comprises over 2 million individual 5-minute granules totalling over 20 TB. While much of these data have been probed by human investigations, the dataset far exceeds one’s capacity for an analysis by visual inspection alone. Moreover, the scope of this dataset poses computational challenges, both in terms of storage and processing resources. Yet, these hurdles are surmountable with modern approaches tailored to big data including cloud storage and modern-day machine learning (ML) techniques.

With this as background and armed with the MODIS dataset and ML tools, we are motivated to study SST patterns across the global ocean and over long time-periods to address the following questions. What are the fundamental patterns and characteristics of SST imagery? When and where do these patterns and characteristics manifest? And, ultimately, what do these patterns reflect about the underlying dynamics?

Our approach is to develop and apply ML techniques originally introduced for natural images (e.g., cats, dogs). By modifying and extending their application to SST imagery (in itself a class of natural images), we may perform novel investigations of the global ocean.

In an earlier study [3], we constructed and applied a probabilistic autoencoder (PAE) [4] nicknamed ULMO to nighttime MODIS L2 SST data. The primary goals of this effort were

J. Xavier Prochaska is an Affiliate of the Ocean Sciences Department at the University of California, Santa Cruz and a Simons Pivot Fellow.

E. Guo was a member of the Department of Computer Sciences at the University of California, Santa Cruz during the formation of this work and is an Affiliate of the Institute of Theoretical Physics, Chinese Academy of Sciences.

P. C. Cornillon is a Professor Emeritus of Oceanography at the Graduate School of Oceanography, University of Rhode Island.

C. E. Buckingham is a Research Assistant Professor in the Department of Estuarine and Ocean Sciences at the University of Massachusetts, Dartmouth. Manuscript received XXX; revised XXX.

¹Including wave-driven currents in the category of sub-mesoscale phenomena, the corresponding horizontal scales must be modified: 0.1-50 km.

to construct a massive dataset for exploration ($\sim 12,000,000$ thumbnails or “cutouts” of dimension $\approx 125 \times 125 \text{ km}^2$) and to identify outliers from the full dataset (i.e., unusual phenomena at the ocean surface). The PAE is an unsupervised ML model which first encodes each cutout into a reduced-dimension latent space (the autoencoder). One then generates probabilistic statements on the cutout distribution, specifically the likelihood of a given cutout occurring within the full distribution reported as a log-likelihood (LL) metric.

After calculating the LL metric for $\sim 12,000,000$ cutouts, [3] showed that the majority of outlier patterns occur within previously known mesoscale eddying regions of the ocean, such as western boundary currents. While this result may have been anticipated by those familiar with physical oceanography, it verified the efficacy of unsupervised ML techniques applied to these massive SST datasets. On the other hand, the ULMO LL metric fails to capture the full complexity of SST imagery—i.e., data with nearly identical LL may arise from distinctly different SST patterns associated with distinct physical processes. This limitation motivates the introduction of a new ML algorithm in this manuscript.

To further address our motivating questions, we build a new model – nicknamed NENYA² – built on the unsupervised ML algorithm termed self-supervised (or contrastive) learning [5]–[11]. This deep learning approach was developed to generate associations amongst imagery with similar characteristics while separating them from data with contrasting nature. In the process, one may explore the diversity of patterns/scenes/etc. that occur within a massive imagery dataset (e.g., [12]). Regarding the ocean, this algorithm offers the opportunity to describe the fundamental patterns of SST fields without introducing rigid rules-based or statistical metrics that may predispose the outcome. Furthermore, it is straightforward afterward to apply any such metric to gain physical insight into the results.

II. DATA AND BASIC METRICS

A. The Cutout Sample

In this manuscript we analyze the nighttime L2 SST Aqua MODIS dataset (<https://oceancolor.gsfc.nasa.gov/data/aqua/>) for the period 2003–2021 inclusive. Our approach to data extraction and pre-processing follow the procedures described in [3]. Specifically, we first generate *patches* with a size of approximately $128 \times 128 \text{ pixel}^2$ that are at least 96% clear, land-free and of good quality. This is a stricter clear criterion than the 95% clear criterion adopted in [3] as subsequent work has identified spurious results from improperly masked clouds or poor in-painting applied to images with $>\sim 5\%$ cloud coverage. We consider this to be the best trade-off between sample size and quality for the analysis presented here.

The patches were drawn randomly from the MODIS granules, restricted to lie within 480 pixels of nadir (to maintain $\sim 1\text{-km}$ resolution) and required to have less than 50% overlap. By allowing for partial overlap, we generate more ‘views’ of a given field.

²The ring of power from the Lord of the Rings associated with water and ULMO.

We then pre-process each patch by: (i) in-painting the bad (flagged) pixels; (ii) median filtering with a 3-pixel window in the along-track direction; (iii) resizing the patch to a $64 \times 64 \text{ pixel}^2$ *cutout* using the local mean of each 2×2 region; and (iv) subtracting the mean temperature to produce an SST anomaly (i.e., SSTa) cutout. Table I lists a small set of the $\approx 8,000,000$ cutouts resulting from the parent sample; the full table is available online.

B. LL and ΔT

To build physical intuition for the results that follow, we introduce several metrics to describe the individual cutouts. Two of these metrics detailed in this sub-section are the ULMO LL metric briefly described in the introduction and the temperature range ΔT defined as the difference in 90th and 10th percentiles of the SST anomaly (SSTa) distribution: $\Delta T \equiv T_{90} - T_{10}$ where T_N denotes the N^{th} -percentile.

For each cutout we calculate the LL metric using the ULMO PAE of [3]. Conceptually, the LL metric describes the relative occurrence of a given image within the ensemble distribution. Here, the distribution is constructed from the set of latent vectors derived from a deep-learning autoencoder designed to capture the features and patterns of SST imagery. To formally calculate LL, the latent space of the autoencoder outputs is transformed to a 512-dimension Gaussian manifold with a normalizing flow. The LL metric is then the sum of the log probability from the 512 Gaussians and the log of the determinant of the transformation. These give the normalization of the LL distribution [13].

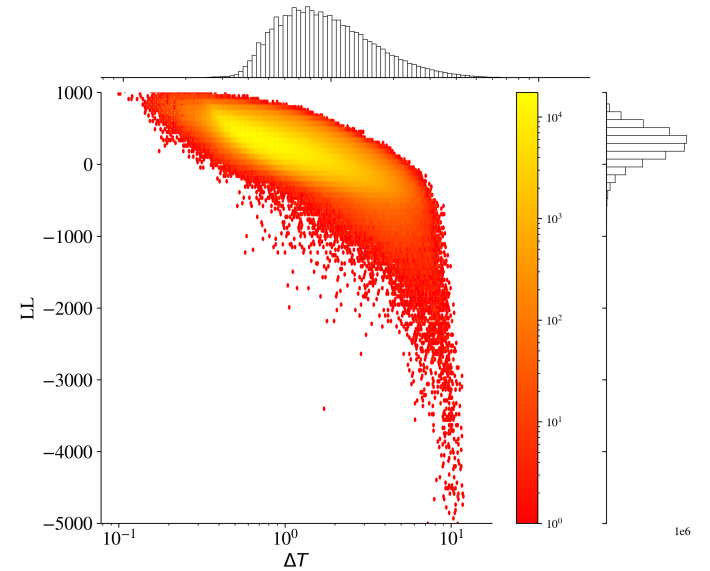


Fig. 1: 2D histogram of the distribution of the LL metric vs. temperature range ΔT , with the color proportional to the log of the counts in each bin. The two distributions are strongly correlated, with the highest ΔT exhibiting the lowest LL values. The marginal distributions are shown as simple histograms. While the LL distribution is well-described by a Gaussian, it does exhibit an asymmetric tail to very low values which are the extreme outliers of the dataset [3].

During their analysis, [3] discovered that the LL values of the cutouts correlate strongly with the temperature range. Put simply, cutouts with high ΔT are rare and yield lower LL values on average. We have calculated and tabulated ΔT for all of the cutouts (Table I), recovering a LogNormal distribution after allowing for a shift and scale,

$$p(\Delta T') = \frac{1}{\sigma_{\Delta T} \Delta T' \sqrt{2\pi}} \exp\left(-\frac{\ln^2 \Delta T'}{2\sigma_{\Delta T}^2}\right) \quad (1)$$

$\Delta T' = (\Delta T - l_{\Delta T})/S_{\Delta T}$ finding $\sigma_{\Delta T} \approx 0.58$, $l_{\Delta T} \approx 0.1$, and $S_{\Delta T} \approx 0.83$. In comparison, the LL distribution is well-described by a Gaussian with mean $\bar{x}_{LL} \approx 270$ and standard deviation $\sigma_{LL} \approx 227$, albeit with a long tail to very low values that define the outlier sample of [3].

Figure 1 shows the LL vs. ΔT bivariate distribution; this reveals the strong correlation; e.g., cutouts with high ΔT exhibit the lowest LL. Despite the correlation, one should not over-interpret Figure 1 to conclude that the LL metric is solely tracking ΔT and therefore could be replaced by it. First, the relationship is not strict; there is a wide range of LL values at a given ΔT . Furthermore, one expects a correlation with LL for any simple metric that describes the features in the imagery. However, no single metric can fully describe the complexity of SST imagery. Stated differently, the complexity of SST imagery belies any single, simple statistic – including the LL measure of our previous work. This motivates, in part, the application of an alternative, deep learning technique. As important, we found that the latent space of ULMO did not group together cutouts with similar patterns. This too motivates the contrastive learning model adopted here.

C. Slopes of the Power Spectrum

Another metric often used to describe structure in SST fields is the slope α of the 1D power spectrum; i.e., the slope of the energy in wavenumber space. When estimated over fine horizontal scales, such as sub-mesoscales (1–50 km), the slope can be descriptive of underlying turbulent processes. For example, classical quasi-geostrophic (QG) turbulence predicts a spectral slope of $\alpha = -3$, surface quasi-geostrophic (SQG) turbulence predicts $\alpha = -5/3$, and an internal-wave continuum predicts $\alpha = -2$ (i.e., for scales less than 10 km and flatter otherwise) [14]–[16].

For the cutouts analyzed here, the smallest scales are expected to be dominated by instrument noise. Therefore, we focus the analysis on larger scales ($\lambda \approx 12 - 50$ km), which corresponds to the upper end of wavelengths associated with sub-mesoscale processes (depending on latitude). Focusing on this range also mitigates, to some extent, contributions to the spectral power at smaller scales due to the multi-detector nature of MODIS. Note, however, that a wavelength of 12 km nominally resolves two eddy-like anomalies of opposite sign, each with radii of 3 km. Since the mixed layer deformation radius of sub-mesoscale anomalies typically exceeds 3 km, this resolves most sub-mesoscale phenomena except perhaps those at polar latitudes.

For each cutout, we determine ensemble averaged power spectra independently for the along-scan (AS) and along-track

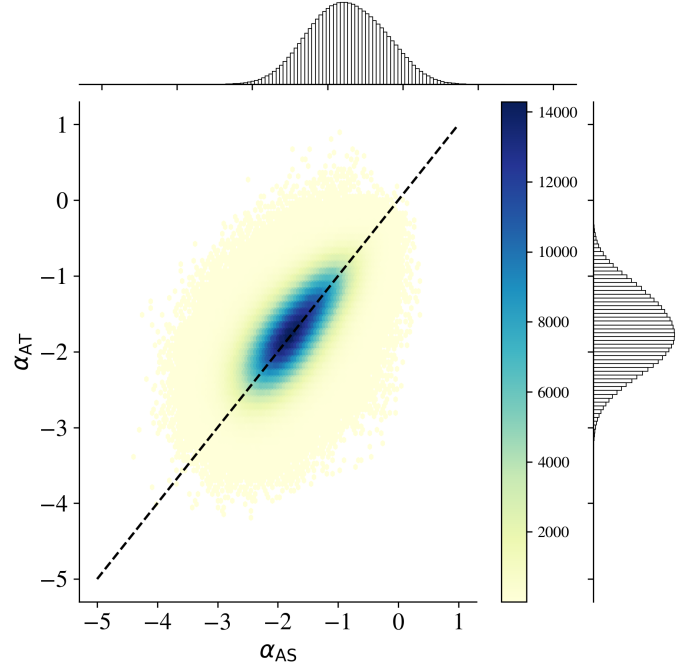


Fig. 2: Bivariate distribution of the along-scan spectral slope α_{AS} versus the along-track α_{AT} , each determined from the portion of the spectra for wavelengths between 12 and 50 km. Typical uncertainties in the measurements are one to several tenths (fitting error only). We find that $> 99\%$ of the cutouts have α_{AS} and α_{AT} within one σ of the estimated error from the 1-to-1 line, indicating their values are highly correlated. The good correspondence between the α_{AS} and α_{AT} implies isotropic motions within the ocean on these physical scales.

(AT) directions. Specifically, for each row (or column) of the cutout, we detrend the data with a linear fit and subtract the mean. We then calculate the fast fourier transform for each row/column and ensemble average the results by row/column. This signal is median filtered with a window of 5 pixels and a power-law is fit to the resultant power spectrum with related uncertainty. We refer to these slopes as α_{AS} and α_{AT} for the AS and AT directions, respectively.

We applied this algorithm to all of the cutout images to calculate α_{AS} and α_{AT} independently (Table I) and also to estimate their uncertainties. Figure 2 plots the two slopes against one another. The marginal distributions of α_{AS} and α_{AT} are well described by Gaussians with nearly identical mean and standard deviations: $\bar{x}_\alpha \approx -1.74$, $\sigma_\alpha \approx 0.5$. Furthermore, we find the slopes for a given cutout agree within uncertainty for the overwhelming majority of cases (i.e., 99% fall within one σ of the mean). This suggests a high degree of isotropy within the dataset.

In the following, we characterize each cutout by a single spectral slope $\alpha_{\min} \equiv \min(\alpha_{AS}, \alpha_{AT})$. Figure 3 shows this quantity versus ΔT , revealing a correlation but with large scatter. Given Figure 1, one notes the α_{\min} is also correlated with LL with the most negative α_{\min} (largest in magnitude) cutouts having preferentially lower LL (as one would expect).

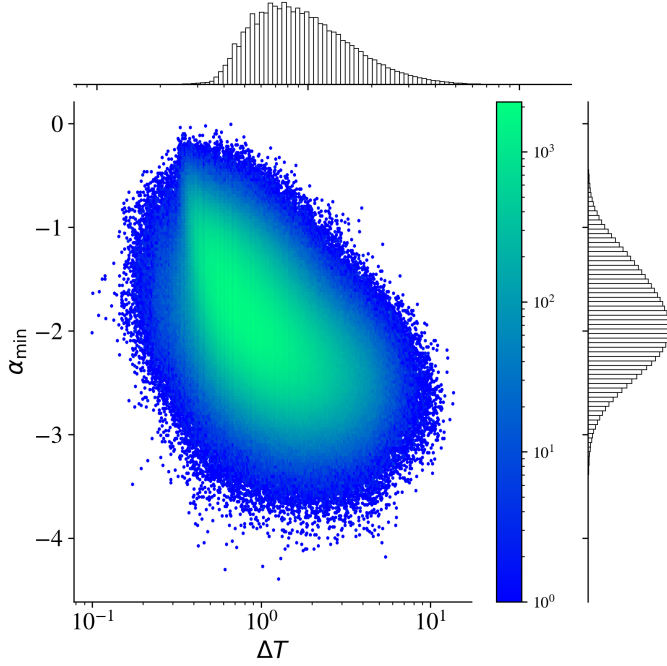


Fig. 3: 2D histogram of the characteristic slope α_{\min} of each cutout vs. ΔT . Regions of the ocean with larger temperature range also tend to exhibit a steeper power spectrum on $\sim 10 - 50\text{km}$ scales, albeit with substantial scatter.

III. METHODOLOGY

A. Overview

Recently, several simple yet powerful self-supervised learning (SSL) frameworks have been proposed to learn useful representations (latents) from high dimensional data sets. This includes so-called contrastive losses which maximize the “similarity” of the views from the same data samples in the latent space [5]–[11]. In our work, we apply the SimCLR framework to analyze the preprocessed cutouts ($64 \times 64 \text{ pixel}^2$ arrays) from the MODIS granules by designing task-dependent augmentations based on our domain knowledge of SST data. The latents obtained by our model are, as designed, a transformation-invariant representation of the SST data. We then study structure in the latent space by projecting into a two-dimensional vector space using a Uniform Manifold Approximation and Projection (UMAP) [17]. The reader is also encouraged to study the methodology developed by [18] using the scattering transform [19].

B. An Introduction to SimCLR

SimCLR is an efficient but simple self-supervised learning model in which a base neural encoder is used to transform the augmented input data point to a latent vector $\tilde{\mathbf{z}}^{(i)}$. By minimizing the contrastive loss, an essential representation can be extracted [7]. The contrastive loss function defined for an augmented sample pair $\{\tilde{\mathbf{z}}^{(i)}, \tilde{\mathbf{z}}^{(i')}\}$ is given by:

$$\text{loss}_{i,j} = -\text{sim}(\tilde{\mathbf{z}}^{(i)}, \tilde{\mathbf{z}}^{(j)})/\tau + \log \sum_{k:k \neq i}^{2m} \exp(\text{sim}(\tilde{\mathbf{z}}^{(i)}, \tilde{\mathbf{z}}^{(k)})/\tau), \quad (2)$$

where $\text{sim}(\tilde{\mathbf{z}}^{(i)}, \tilde{\mathbf{z}}^{(j)})$ is defined as the dot-product similarity of the latent pair $\{\tilde{\mathbf{z}}^{(i)}, \tilde{\mathbf{z}}^{(j)}\}$, namely the output of the neural encoder, and τ is a hyper-parameter used to fine-tune the amplitude of the similarity. In essence, the contrastive loss (2) is just the rescaled similarity of the sample pair with a batch normalization penalty term.

For our model, we use ResNet-50 [20] as the encoder because unsupervised learning favors models with larger capacity [8]. We do not employ a projection head, and the latents generated by the encoder are passed directly to the contrastive loss function, without additional nonlinear transformation. The advantage of discarding the projection head is that a reasonable similarity can be defined for the latents obtained by the encoder during the evaluation step³. After some experimentation, we have set the dimensionality of the latent space to 256.

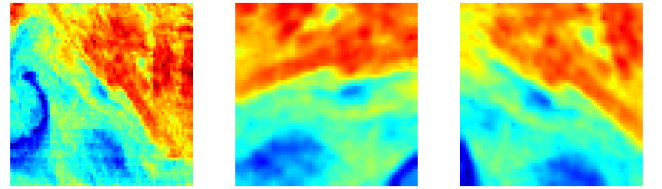


Fig. 4: The left panel is the ‘raw’ cutout input to the augmentation module and the other two images are a pair of augmented samples. The first (center image) was randomly flipped about the vertical axis and then rotated by $\approx 320 \text{ deg}$ and jittered by 5 pixels vertically. The second (right image) was not flipped, was rotated by $\approx 18 \text{ deg}$ and jittered by 2 pixels horizontally and vertically. Each augmented image was then cropped by the inner $40 \times 40 \text{ pixel}^2$, resized to $64 \times 64 \text{ pixel}^2$ and demeaned.

C. Augmentations

The random augmentation module is crucial for model performance and affects the nature of the patterns captured in the latent space. After experimenting with standard augmentations intended for natural images, we refined based on the following domain considerations: invariance to (i) rotation, (ii) translation, and (iii) reflection. The reason for the first consideration is that the MODIS L2 data product is not oriented parallel to either the zonal or meridional directions. Moreover, while there may be scientific motivations for preserving orientation when analyzing SSTa fields more generally, the north-south gradient in solar insolation and in beta has little impact on the gradient in SST at the scales of interest here ($< 80 \text{ km}$). This is supported by Figure 2. The reason for the second consideration is that we desired a description of the SST patterns that is insensitive to small spatial shifts. That is, viewing the region offset by, for example, 10 km typically results in a similar

³If the project head is used, the similarity in the contrastive loss is defined by the dot-product of the transformed latents.

pattern. Finally, the impetus for the third consideration is that we suspect a reflection or “mirror image” of the original cutout should capture all of the same information. As an aside, we also considered inverting the SSTa field (i.e., turning warm to cold), but did not do so in the end since some dynamic features have a physical preference (e.g., mesoscale currents are generally warmer than the surrounding waters).

With these considerations in mind, we imposed the following augmentations in this order:

- **Random Flip:** We randomly flip the image in each dimension with a 50% probability (e.g., a 25% probability of no alteration).
- **Random Rotation:** We rotate the cutouts with random angles which are uniformly sampled from $\theta = [0, 2\pi]$. The new image maintains $64 \times 64 \text{ pixel}^2$ with data rotated ‘off’ now lost and otherwise empty regions imputed with 0 values.
- **Random Jitter and Crop:** We randomly select a new image center uniformly offset from the original by up to 5 pixels in each dimension. We crop the original image around the translated center to $40 \times 40 \text{ pixel}^2$ to eliminate the inclusion of the zero-filled portions introduced by the rotation. Last, we resize the cropped image back to the original grid size of $64 \times 64 \text{ pixel}^2$.
- **Demean:** The final image is demeaned.

Figure 4 shows a representative cutout and two of its randomly augmented samples. These were randomly flipped, rotated and jittered, and then cropped to the inner $40 \times 40 \text{ pixel}^2$, resized to $64 \times 64 \text{ pixel}^2$ and demeaned. Our SSL model, which operates solely on augmented images, learned to recognize these as similar and to distinguish their underlying patterns from those of other cutouts.

D. Training and Evaluation

For training of the model, we randomly selected 600,000 cutouts from the full set. For validation, we randomly selected another 150,000 cutouts. With 4 GPUs, we train NENYA with a batch size of 256. To monitor the contrastive lost on the validation set, we find that after ≈ 5 epochs of training, the model learns good representations of the training data set. SSL models benefit from bigger batch sizes; our experimentation showed good performance for sizes of 256 or more.

In Fig. 5, we show the learning curves for the NENYA model in the training and validation process. Learning loss decreases rapidly with training batch number suggesting that the model converges well.

We then evaluated all 21 years of MODIS cutouts, generating and recording a unique 256-dimension latent vector for each. These constitute the learned representations of the fundamental SST patterns of the imagery on scales $\leq 80 \text{ km}$.

E. UMAP Dimensionality Reduction

While the latent vectors encode the features characterizing the SST patterns, it is difficult as humans to visualize and explore this 256-dimension latent space. Therefore, we have implemented the UMAP algorithm to further reduce the latent

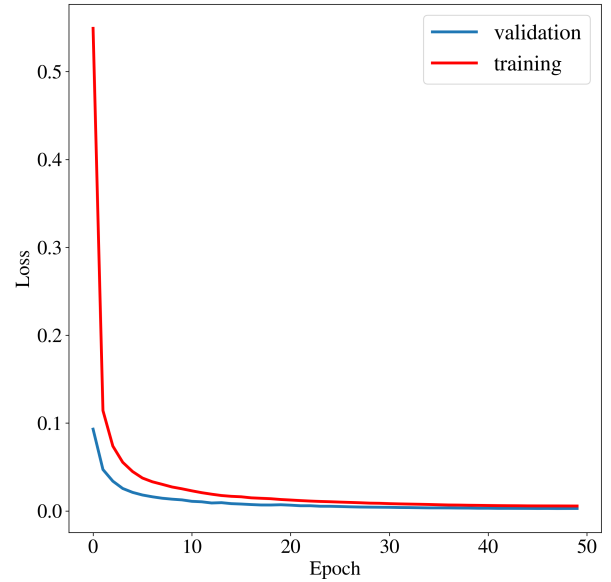


Fig. 5: Learning curves (batch losses) for the training set (red) and validation set (blue) for our SSL model. The model achieves a low loss after ≈ 5 epochs and has effectively converged after ~ 20 .

space to two dimensions (U_0, U_1). We adopt the default parameters of the UMAP package [21] throughout.

We emphasize that neither of the parameters U_0, U_1 need to have a direct, physical meaning or analogue. These are only statistical in nature, although they are tuned to separate the latent vector space and therefore track the fundamental patterns of SST imagery. Only the 256 dimension latent vectors are the full model representation of the underlying patterns—i.e., the two-dimensions of this UMAP are (by design) a limited representation of the full complexity. Nevertheless, we find that by applying the UMAP to a series of ΔT sub-samples that we describe a majority of the diversity within the dataset. The following section explores the outputs of this procedure and also their scientific implications.

IV. RESULTS

The previous section described the deep learning methodology introduced to analyze the MODIS L2 dataset. Specifically, the NENYA model was trained to associate images with similar SST patterns on scales of $\approx 80 \times 80 \text{ km}^2$ and smaller, while separating these from dissimilar images. The resulting 256-dimension latent space therefore represents a new method or *vocabulary* for describing SST imagery on sub-mesoscales. This section examines a portion of the vocabulary describing the rich complexity of SST imagery. To facilitate the exploration, we map the 256-dimension latent space to a reduced basis (two dimensions) for the full dataset and subsets in ΔT .

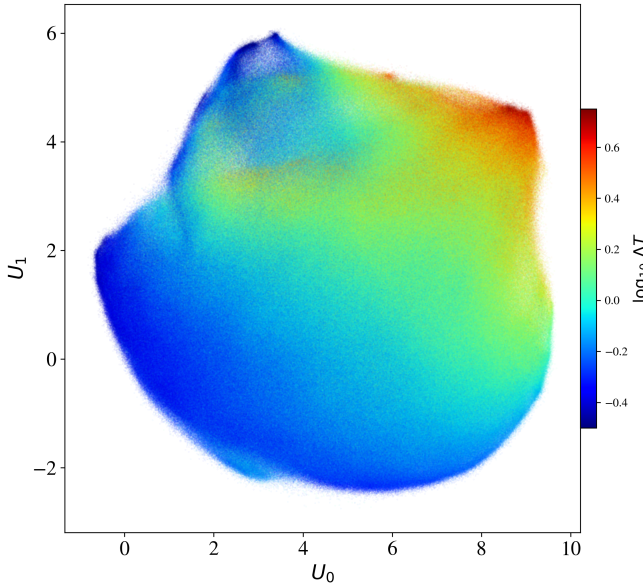


Fig. 6: UMAP two-dimensional manifold description of the latent-vector space (256-dimensions) which represents the fundamental SST patterns. Each cutout is shown as a dot in the space, color-coded by $\log_{10} \Delta T$ of the cutout.

A. Full Sample

We begin by examining the full sample, applying the UMAP algorithm to all of the $\approx 8,000,000$ latent vectors. Figure 6 shows the reduction of SST patterns into two dimensions for the full set of imagery, color-coded by $\log_{10} \Delta T$. The relatively uniform distribution indicates the SST imagery exhibits a smooth continuum of patterns and features as opposed to “clusters” of discrete classes. Furthermore, by coloring the data by ΔT , we emphasize that this property is a dominant “axis” in separating the SST imagery (here oriented at $\sim 45^\circ$ to the U_0, U_1 axes). The strong ΔT dependence is relatively obvious in hindsight; having removed the first moment in SST (the mean), the second moment (variance) remains a principle characteristic of each SSTa cutout. And while ΔT has physical significance for the ocean (e.g., high values preferentially arise in dynamically active regions), we wish to discriminate the patterns based on finer features. These are captured in the full 256-latent space and we access them in the following section by sub-dividing the full sample into ΔT intervals and then reducing each sub-sample with its own UMAP algorithm.

Before proceeding, we further examine the UMAP results for the full dataset via a gallery of representative images. We have gridded the U_0, U_1 space and selected a random cutout from within each grid cell; these are plotted in Figure 7. As designed, NENYA has effectively separated the SST imagery by their patterns. Qualitatively, the data is highly uniform in the lower left region of the UMAP space ($U_0, U_1 \approx 0, -1$) and one observes increasing complexity as one moves away from this “origin”. Greatest structure is evident at high U_0, U_1

values, with patterns characterized by water masses of high positive and negative SSTa separated by a sharp front. These are likely associated with strong ocean currents, such as the Gulf Stream, Kuroshio, and Antarctic Circumpolar Current, regions of relatively large changes in shallow bathymetry often encountered near the edge of the continental shelf and in vertically stratified regions with strong winds such as off the Isthmus of Tehuantepec.

B. The Fundamental Patterns of SST

In the previous sub-section, we showed that reducing the full set of latent vectors to two dimensions with a UMAP embedding primarily separated the SST patterns by ΔT . While informative, this does not express well the great diversity within the dataset. Therefore, we proceeded to generate a unique UMAP embedding of the latent space for sub-samples of the cutouts separated by ΔT . Specifically, we measure ΔT from the inner $40 \times 40 \text{ pixel}^2$ regions of each cutout which corresponds to the regions augmented by the NENYA model (see § III-C). We then consider ΔT bins as follows:

- (a) $\Delta T = 0 - 0.5 \text{ K}$; 2635727 cutouts; Figure 17
- (b) $\Delta T = 0.5 - 1 \text{ K}$; 3288103 cutouts; Figure 9
- (c) $\Delta T = 1 - 1.5 \text{ K}$; 1126838 cutouts; Figure 18
- (d) $\Delta T = 1.5 - 2.5 \text{ K}$; 535038 cutouts; Figure 19
- (e) $\Delta T = 2.5 - 4 \text{ K}$; 126576 cutouts; Figure 20
- (f) $\Delta T > 4 \text{ K}$; 18317 cutouts; Figure 21

This otherwise arbitrary binning was chosen to minimize ΔT as a defining factor in the analysis while maintaining large samples of cutouts. Figure 8a shows the UMAP representation of the $\Delta T = 0.5 - 1 \text{ K}$ sub-sample colored by ΔT . While there is structure in the domain that correlates with ΔT , it is no longer monotonic and cutouts with the full range of ΔT are located throughout (the standard deviation in ΔT is $\sigma(\Delta T) \approx 0.13 \text{ K}$; see Figure 8b).

Figure 9 shows a gallery of randomly selected cutouts for the $\Delta T = 0.5 - 1 \text{ K}$ subset at their binned U_0, U_1 values (restricted to areas with at least 1000 cutouts per bin). Examining the figure, one observes a great diversity in the patterns as one travels throughout the UMAP space. One identifies features for which SSTa contours are predominantly linear (e.g., at low U_0, U_1), curved (e.g., $U_0, U_1 \approx 8, 2$) or amorphous (e.g., $U_0, U_1 \approx 4, 4$), patterns with apparent symmetry about an axis (e.g., $U_0, U_1 \approx 0, 2$) and those without any discernible structure (e.g., $U_0, U_1 \approx 9, 1$).

To build additional intuition for the patterns resolved by NENYA, we show a series of properties of the cutouts in Figure 8, binned by U_0 and U_1 . The characteristic most highly correlated with the pattern distribution in the UMAP embedding is the absolute latitude $|\text{latitude}|$ (Figure 8e). Given the $|\text{latitude}|$ dependence for the radius of deformation, this suggests the patterns have been separated by the dominant feature scale, especially along the U_1 dimension. Visual inspection supports this hypothesis to an extent, e.g. the patterns with largest-scale variance have lower U_1 . On the other hand, cutouts with the smallest scale features arise at high U_0 and low U_1 corresponding to mid-latitudes. These also have the highest cloud coverage fraction (Figure 8d)

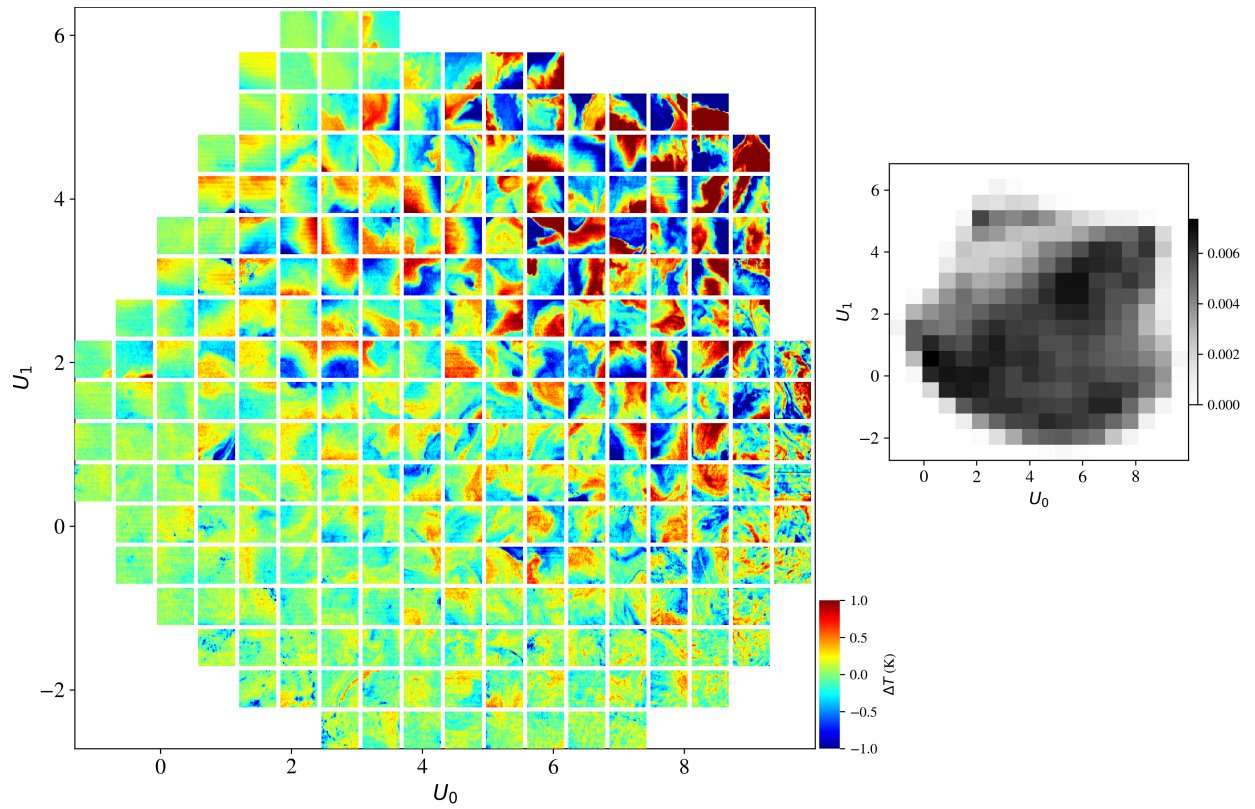


Fig. 7: Gallery of cutouts, each one selected at random from a gridded U_0, U_1 space for the full dataset. The data show increasing structure and complexity as one transitions from the lower left ($U_0, U_1 \approx [0, -1]$) to the upper right of the domain. Along this same direction the average ΔT is increasing, i.e., this embedding is especially sensitive to the cutout ΔT . The gray histogram on the right describes the relative frequency of cutouts at each location in the UMAP domain.

and close inspection of individual cutouts reveals small-scale blemishes characteristic of clouds. We believe these have been missed by the standard screening algorithm and future work may leverage NENYA to flag corrupt data and/or improve the screening process.

Figure 8c shows the median spectral slope α_{\min} which varies across the domain. The values are all negative, indicative of reduced energy at high wavenumbers and, thus, consistent with all theories of geophysical turbulence [14]–[16] (cf. section II-C). The pattern dependence on α_{\min} is complex with very differing imagery having similar median α_{\min} . Similarly the standard deviation of α_{\min} is large (not shown). Together, these indicate α_{\min} is an incomplete descriptor of SST patterns and features.

To better guide analysis presented in the following section, Figure 10 shows the UMAP with several sub-regions annotated to approximately demarcate several types of patterns: those with temperature variance predominantly on the largest scales (solid annotation), cutouts with an “energetic” spectrum showing structure at a range of scales (dashed ellipse), and noisy patterns with structure predominantly on the smallest scales (dash-dot ellipse).

Galleries for the other ΔT sub-samples are provided in the Appendix (Figures 17–21). Together with Figure 9 these six UMAP spaces span the full diversity of SST patterns, as

encoded in the full SSL latent space. With NENYA, we have constructed a vocabulary that encodes the complex language of SST imagery on sub-mesoscales. Any SST cutout drawn from the MODIS L2 dataset maps directly to one of the 6 galleries and is—by design—very similar to its neighboring cutouts in UMAP space. This enables novel exploration of the data—e.g., the ability to define and investigate regions of the ocean with special or unique SST signatures.

Before proceeding, however, a cautionary note is warranted. Because a unique UMAP embedding is generated for the latent vectors in each ΔT bin, the meaning of the U_0 and U_1 axes likely differ from one ΔT bin to the next. Having said this, we note that with the exception of the gallery for $\Delta T = 0 - 0.5$ K (Fig. 17) all of the galleries show the complexity (e.g., curvature of SSTa contours) increasing as U_1 increases. That is, setting aside the effect of ΔT , this may be the primary distinguishing characteristic of the fields identified by NENYA.

V. APPLICATIONS AND DISCUSSION

In the previous section, we presented the fundamental patterns of SST imagery learned by the NENYA model on scales smaller than ≈ 80 km. We now demonstrate several applications enabled by constructing this vocabulary to describe the complex patterns of these data. In particular, one may explore the nature and origins of specific patterns across

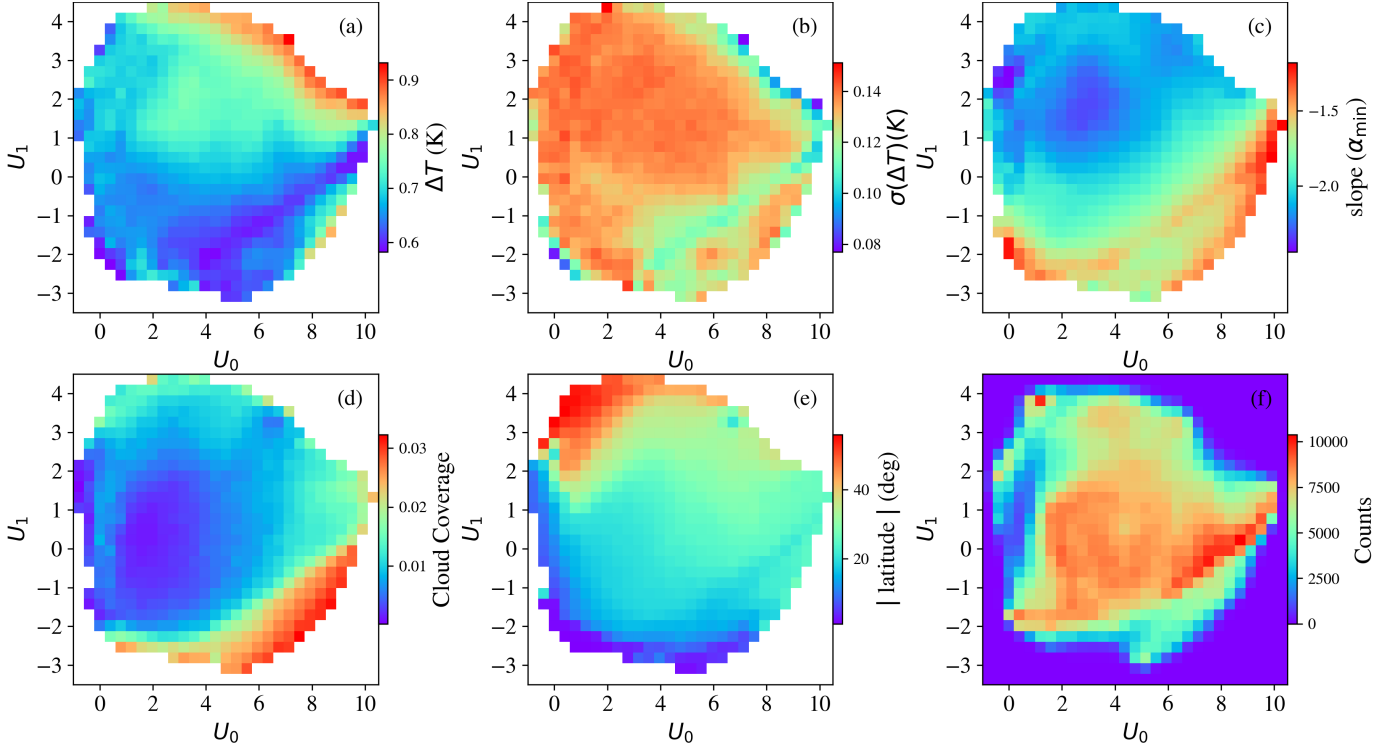


Fig. 8: Binned evaluations in the UMAP embedding for properties of the cutout subset with $\Delta T = 0.5 - 1$ K. Panels (a), (c), (d), and (e) show the median value of ΔT (with a linear color scale because of the relatively small temperature range compared with the \log_{10} scale used for Figure 6), α_{\min} , cloud coverage, and the absolute latitude of the cutouts respectively. Panel (b) presents the standard deviation in ΔT and panel (f) records the number of cutouts in each bin.

the ocean or the patterns that manifest in select regions, and explore temporal variability. In this section, we focus on the $\Delta T = 0.5 - 1$ K subset and emphasize that the primary results are largely insensitive to this choice.

A. Geographical Exploration

A defining characteristic of data collected by remote sensing satellites such as Aqua is their global coverage of the ocean. Using the NENYA model, we may select specific patterns of SST and reveal their global geographic locations. We may then assess commonality (or otherwise) between the processes that generate them. Alternatively, we may select specific local regions to highlight the SST patterns that define them. Here, we consider each of these approaches in turn.

1) **Global:** To perform a global analysis, we have divided the surface of the ocean using the Hierarchical Equal Area isoLatitude Pixelation (HEALPix) procedure which tessellates a spherical surface into equal-area curvilinear quadrilaterals [22]. Specifically, we adopted $n_{\text{side}}=64$, which divides the globe into $\approx 50,000$ HEALPix cells each with approximately $100 \times 100 \text{ km}^2$ area. We then perform statistics on the cutouts which occur within each of these HEALPix cells.

As a first example, we consider cutouts with patterns that exhibit temperature variance predominantly on the largest scales of our augmented images (i.e., 80 km). Specifically, we select the portion of the UMAP domain corresponding to $\Delta T = 0.5 - 1$ K with $U_0 = [0, 2]$ and $U_1 = [-2.5, -0.3]$. This

includes $\approx 225,000$ cutouts from the lower left corner of the domain (Figure 10; solid rectangle).

Let us now define a *relative fraction* f_r for each HEALPix which is the ratio of two fractions: (i) f_H , the fraction of cutouts in the HEALPix which lie within the UMAP rectangle defined above and; (ii) f_T , the total fraction of all cutouts for the given ΔT range that lie within the same rectangle. We then calculate

$$f_r \equiv \frac{f_H}{f_T} \quad (3)$$

for each HEALPix cell, ignoring cells with fewer than 5 cutouts. Small values of f_r indicate the pattern (characterized in UMAP-space) occurs rarely within the HEALPix relative to the average, and vice-versa.

Figure 11 presents the geographic distribution of f_r for $U_0 = [0, 2]$ and $U_1 = [-2.5, -0.3]$ in the $\Delta T = 0.5 - 1$ K bin (Figure 10; solid rectangle). Focusing on geographical regions with an enhanced incidence of these patterns ($f_r > 1$), we find the majority occur in large, coherent regions ($\gg 100 \text{ km}$), i.e., much larger than the cutouts analyzed by the NENYA model. In this case, the SST patterns have tagged processes on scales substantially larger than the sub-mesoscale. One also notes that these areas are primarily at low latitudes; this follows physical intuition that the high radius of deformation near the equator leads to larger-scale features. We briefly describe processes that may generate the underlying SST patterns in several of these regions.

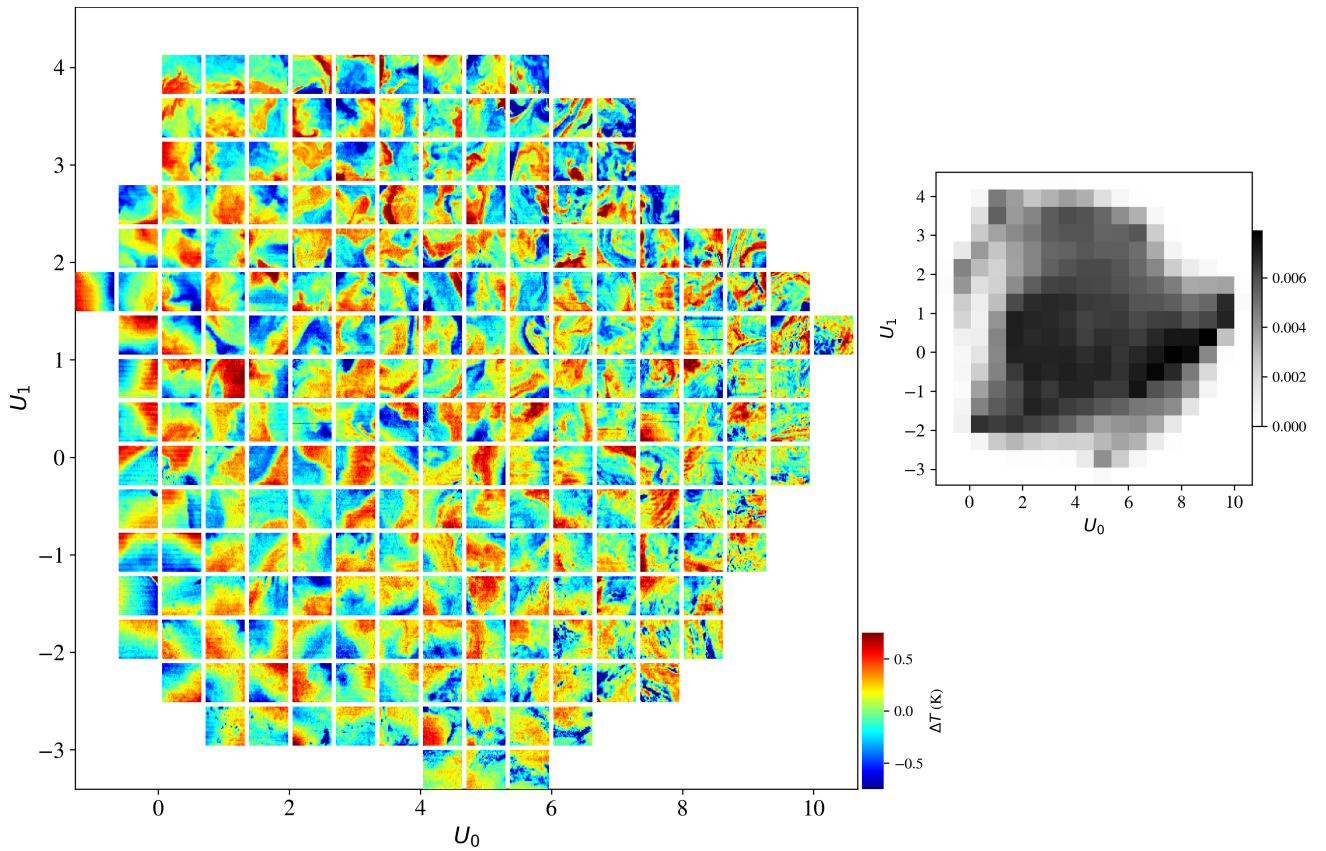


Fig. 9: As in Figure 7 but for the UMAP embedding of the $\Delta T = 0.5 - 1$ K sub-set of cutouts (3,320,395 in total; a cutout is only shown in U_0, U_1 bins where there are at least 1,000). In contrast to the full set where the UMAP space was largely defined by the ΔT of each cutout, this embedding separates the patterns by finer features. Spanning the domain, one identifies a diversity of patterns with structure on the full range of scales. As designed, NENYA has effectively generated a vocabulary to describe and distinguish between the fundamental patterns of SST.

Two of the largest regions with high f_r in Figure 11 are along the eastern equatorial Pacific and Atlantic. These areas are commonly referred to as the Pacific and Atlantic equatorial cold tongue (ECT), and are of interest to climate studies owing to their impact on air-sea interactions (e.g., [23], [24]). Briefly, ECTs are believed to result from upwelling associated with northward wind stresses in the eastern portion of each basin. This water is then forced by zonal winds to propagate westward [23]–[25]. Figure 11 indicates the ECTs exhibit similar SST patterns that span several thousands of kilometers along the equator, stretching to $\approx 180^\circ$ W in the Pacific and nearly across the entire Atlantic. The Pacific ECT is confined to a meridional extent of approximately $\pm 5^\circ$. In the following section, we examine its seasonal variation.

To the north (at $\approx 10^\circ$ N) and distinct from each ECT is an additional region of high relative frequency, one off the coast of Central America and another off the coast of western Africa. Each region is characterized by (seasonal) coastal upwelling and poleward currents [26], [27]. For example, in the Eastern Tropical Pacific, off the coast of Central America, seasonally-varying and intense wind “jets” generate westward-propagating Rossby waves and/or mesoscale eddies in this region [28]. The SST patterns accentuated in this region,

however, are not characteristic of such dynamics (see below); we expect the large-scale temperature variance arises from different processes hereto not explored by previous studies. The Atlantic region, meanwhile, corresponds approximately to the “shadow zone” of the eastern tropical North Atlantic and the so-called Guinea dome below it [27], [29]. These have weak circulation and our results suggest, unexpectedly, that the prevailing SST signatures within them are large-scale temperature variations.

Distinct from the enhanced regions at lower latitudes are the waters off the Patagonia shelf. This region is characterized by a shallow continental shelf and the nearby confluence of two strong currents: the equatorward-flowing Malvinas current which meets the poleward-traveling Brazilian current at $\approx 40^\circ$ S. The circulation on the shelf is predicted (and observed) to be relatively weak [30]. We hypothesize that bathymetry plays a leading role in the generation of the observed SST patterns, which is supported by the orientation of the large-scale temperature variance in the cutouts. We also note that the waters off eastern Africa at $\approx 5^\circ$ N share features common to the Patagonia shelf [31]; perhaps bathymetry is a driving factor for its high f_r , as well.

In an effort to contrast the geographical distribution of the

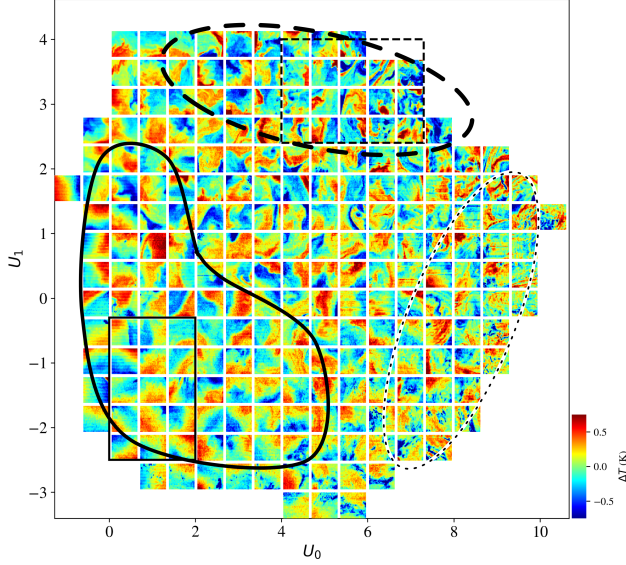


Fig. 10: A reproduction of the UMAP domain in Figure 9 but now annotated to highlight regions of interest in the UMAP space. The annotations approximately designate regions where the patterns show: (solid-line annotation) temperature variance predominantly at the largest wavelengths; (dashed-line ellipse) temperature variance reflective of an energetic spectrum, e.g. non-linear, or turbulent motions; and (dash-dot ellipse) patterns with “noisy” features, predominantly on the smallest scales. Meanwhile, the black rectangles (solid and dashed) in the left panel indicate the portions of the UMAP domain analyzed in Figures 11 and 12.

large-scale SST patterns of Figure 11 with that for cutouts suggesting a significantly shorter range of scales, we now focus on SST patterns for which $\Delta T = 0.5 - 1$ K with $U_0 = [4, 7.3]$ and $U_1 = [2.4, 4]$ (Figure 10; dashed rectangle). Their complex patterns are suggestive of regions in which non-linear, sub-mesoscale dynamics (e.g., eddies and filaments) and/or ageostrophic turbulence are to be found.

Figure 12 presents the relative frequency f_r of these patterns. All of the geographical regions in Figure 11 with high relative fractions now have low f_r , and an entirely distinct set of locations with high f_r appear. These are primarily poleward of 20° deg and may be divided into four main groups. (1) waters associated with strong open-ocean currents (e.g., the Brazil-Malvinas confluence, the Gulf Stream, the Kuroshio, the Agulhas Retroflexion); (2) enclosed or semi-enclosed seas (e.g., parts of the Mediterranean, the Sea of Japan, the Okhotsk Sea, the southern end of the Red Sea, the northern half of the Gulf of Mexico, the Baltic Sea); (3) eastern boundaries of most ocean basins in the subtropics (e.g., off California and Mexico, Chile, Northwest Africa); and (4) anomalous regions equatorward of 22.5° : the Bay of Bengal and the retroflexion of a portion of the South Equatorial Current into the Equatorial Countercurrent off of northern Brazil and French Guiana.

As noted above the first group is associated with strong currents and comprise regions where eddies frequently form

(e.g., [32]). Several are also noted regions of strong upwelling, e.g., coastal California [34]. Neither of these are a surprise. By contrast, a significant fraction of virtually all major enclosed or semi-enclosed seas comprise cutouts for which SST contours show signs of relatively small spatial scales while these regions show little to no signs of long wavelength contours (Fig. 11). Is this because topography is complex in these regions exerting significant control over circulation? Or, maybe land constrains the flow both of currents and winds resulting in smaller scale motion? Regardless, the implications here are intriguing.

We may speculate—given the randomly-selected cutouts presented in UMAP-space—that the SST patterns with $f_r \gg 1$ Figure 12 trace regions of active frontogenesis, frontolysis, and frontal instabilities at scales defined as sub-mesoscale ($\lambda < 50$ km) and therefore enhanced ageostrophic turbulence. It is an active area of interest for the authors to connect such processes to the specific SST patterns defined by NENYA.

Last, a visual inspection of the cutouts with high U_0 and low U_1 in the dotted ellipse of Figure 10 shows signatures of clouds, e.g., patterns of speckled, cooler patches. These are primarily cases that passed through the cloud-screening algorithms [35] of the R2019.0 MODIS processing. In this respect, our NENYA model has efficiently identified corrupt fields. We have examined the geographic distribution of these cutouts and found they generally track the overall distribution of data, although there is a preference for mid-latitudes.

2) **Local:** We may effectively invert the above analysis to examine the SST patterns that are dominant in select geographical regions. As an example, Figure 13 shows the relative frequency, corresponding to the $\Delta T = 0.5 - 1$ K subset, of SST patterns in the Pacific ECT (black dashed rectangle in Figure 11). For this analysis, we have divided the UMAP domain into 18×18 equal-spaced bins that span 99.9% of each dimension ($\Delta U_0 \approx 0.65$ and $\Delta U_1 \approx 0.45$). We then calculate a *relative frequency* of occurrence f_b , defined as the frequency of cutouts for the region in each bin f_R divided by the frequency measured for the entire ocean f_O :

$$f_b \equiv \frac{f_R}{f_O} . \quad (4)$$

High f_b values therefore indicate SST patterns that are more characteristic of the region than that of the global ocean. These f_b maps are the SST “fingerprints” of the regions specifying the SST patterns they preferentially manifest.

Examining Figure 13, we find the Pacific ECT shows an excess of SST patterns with low U_1 ; these are a combination of cutouts with large-scale structure and cutouts with significant “blemishes”, which we identify as unmasked clouds. The patterns with $f_b < 1$ for the Pacific ECT, meanwhile, are those with temperature variance across a range of scales including small scales. We conclude it is very rare for such fluctuations to occur in this region, i.e., the westward propagation of the ECT is stable against such instabilities. Additional exploration reveals that features likely associated with tropical instability waves that occur along the meridional periphery of the ECT [36] have larger scale gradients and higher ΔT (e.g., at $U_0, U_1 \approx 6, 8$ in Figure 19).

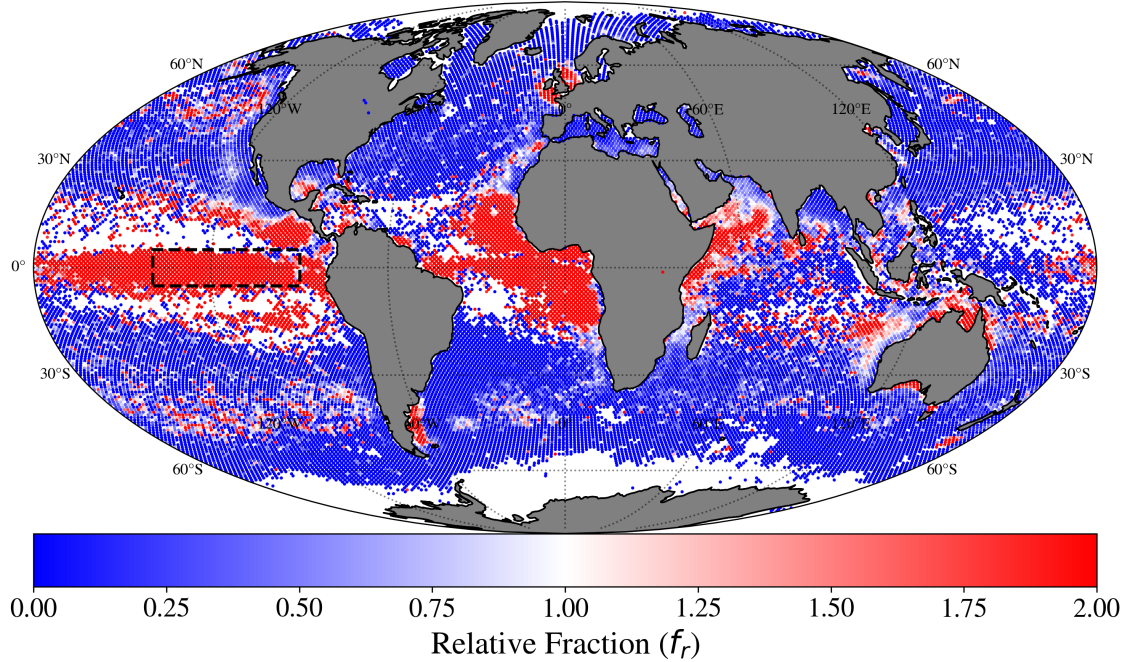


Fig. 11: Relative fraction f_r of SST cutouts with temperature variance predominantly on large scales (≈ 80 km) from the $\Delta T = 0.5 - 1$ K subset (specified by the dashed rectangle in Figure 9). A low value (blue) implies that the geographic location, with area of $\approx 100 \times 100$ km², rarely exhibits such patterns while $f_r \geq 1$ (pink/red) indicates an excess. Gray regions indicate land. The figure reveals that large-scale patterns arise primarily at lower latitudes (e.g., the equatorial Pacific and coastal Africa), but also along the Patagonia shelf and Northern Sea. Regions with fewer than 5 cutouts in the ΔT interval are indicated in white and have not been included in the analysis. The dashed black rectangle is the focus area for Fig. 13.

Two more local regions are presented in Figure 14. These highlight two areas from Figure 12: one with a high relative fraction (the Gulf Stream near New England) indicative of a highly dynamic region, and one with low f_r (the equatorial Indian Ocean). The dominant SST patterns of the Gulf Stream are drawn from the high U_1 portion of the UMAP domain (Figure 14), especially the energetic region annotated in Figure 10 (dashed ellipse). These patterns show the highest degree of complexity with temperature variance at a range of scales, and features with strong curvature, and strong gradients. By the same token, the Gulf Stream avoids the regions of the UMAP domain where cutouts show predominantly large-scale or small-scale structures (solid and dotted annotations respectively in Figure 10). Together, the f_b distribution in the upper panel of Figure 14 identifies the SST patterns that manifest in highly dynamic regions (e.g., near and within western boundary currents).

The lower panel of Figure 14 describes the SST patterns prevalent in the equatorial Indian Ocean. These occur predominantly within the lower-right portion of the UMAP domain (dotted annotation in Figure 10). This region contains primarily

cutouts with isolated, cooler patches (e.g., unmasked clouds) and those dominated by small-scale variance. Likewise, it is very rare for this portion of the Indian Ocean to exhibit temperature variations on medium to larger scales.

B. Temporal Change

In addition to the extensive (global) geographic coverage afforded by remote sensing observations, the MODIS dataset now spans nearly two decades of daily observations. This permits a time-series analysis of the incidence of SST patterns characteristic of particular dynamics. We consider both long-term (i.e., inter-annual) and short-term (seasonal) trends in select regions.

Returning to the Pacific ECT, we perform a time-series analysis for its prominent SST patterns. We define these patterns as the portion of the UMAP domain for the $\Delta T = 0.5 - 1$ K sample that have a relative frequency $f_b > 1.5$, i.e., the red regions in Figure 13. For each month of each year in the dataset, we calculate the fraction of cutouts f_c in that portion of the UMAP domain. If there are fewer than 10 cutouts in a given month and year, that time-stamp is ignored.

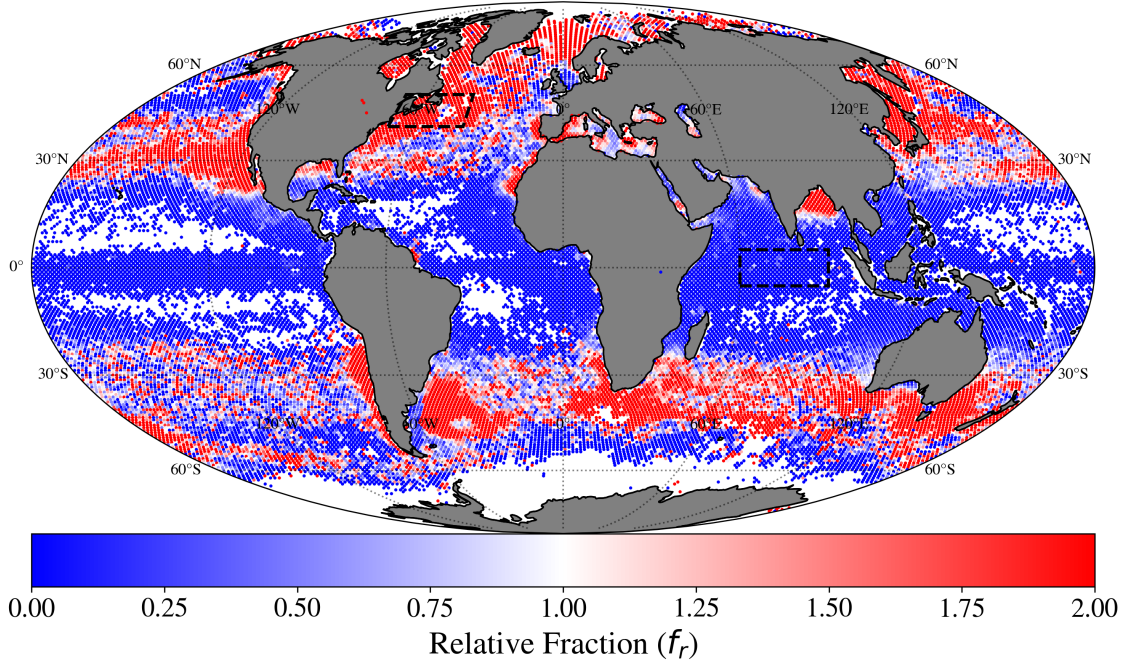


Fig. 12: Same as Figure 11 but for SST patterns with structure across a range of scales and from the $\Delta T = 0.5 - 1$ K subset (specifically $U_0 = [4, 7.3]$ and $U_1 = [2.4, 4]$). The regions that show a high fraction of these turbulent patterns are predominantly those influenced by western boundary currents and areas generally known to show frequent eddy formation and propagation [32]. Strong upwelling may also generate these patterns in select regions: coastal California, western Africa, Chile. We also emphasize the the Bay of Bengal whose dynamics are driven by qualitatively different processes [33]. Dashed black rectangles on the Gulf Stream near New England and the equatorial Indian Ocean are the focus areas for Fig. 14.

The time-series of f_c and its seasonal and inter-annual analysis is plotted in Figure 15. The time-series analysis models the data assuming a linear trend for any inter-annual variation and 11 free parameters for the months January–November to assess seasonal variations (the results are relative to December). A strong seasonal component is apparent with the boreal summer months (May–September) dominant and with the ECT suppressed from February–March inclusive. The enhancement has been associated with the intensification of the Pacific ECT by air-sea interactions [37], [38]. There is no significant linear inter-annual trend, but we do observe that the near-disappearance of the ECT (low f_c) in February/March has been intensifying over the past ~ 10 years.

Turning to a portion of Gulf Stream near New England, we isolate the cutouts with $f_b > 1.25$ in the upper panel of Figure 14 which are those with complex patterns. Similar to the Pacific ECT, the primary SST patterns of the Gulf Stream exhibit a strong seasonal dependence (Figure 16). Its seasonal trend, however, is (coincidentally) out-of-phase with the ECT showing the highest f_c in winter months and a great deficit in mid-summer. The latter may occur as a significant seasonal

thermocline is formed in the area to the north and west of the Gulf Stream effectively obscuring the more turbulent waters beneath.

VI. SUMMARY AND CONCLUDING REMARKS

We have designed a deep, contrastive learning model to reveal and resolve the fundamental patterns of SST for the global ocean on scales of $\approx 80 \times 80 \text{ km}^2$ (i.e., sub-mesoscale). This NENYA model is intentionally invariant to vertical and horizontal flips, rotations, and small translations. We trained NENYA on 600,000 random cutouts from the MODIS L2 night-time dataset in the years 2003–2021 inclusive. To readily explore the 256-dimension latent space that defines the complexity of SST patterns, we bin the cutouts by ΔT —the size of its 90% SST interval—and generated a UMAP transformation of the latent vectors to 2-dimensions.

We confirmed that NENYA has successfully separated the SST patterns in this 3-dimensional space (one for ΔT , and 2 for each UMAP) to describe the full complexity of SST imagery. We identify SST patterns with structures on scales ranging

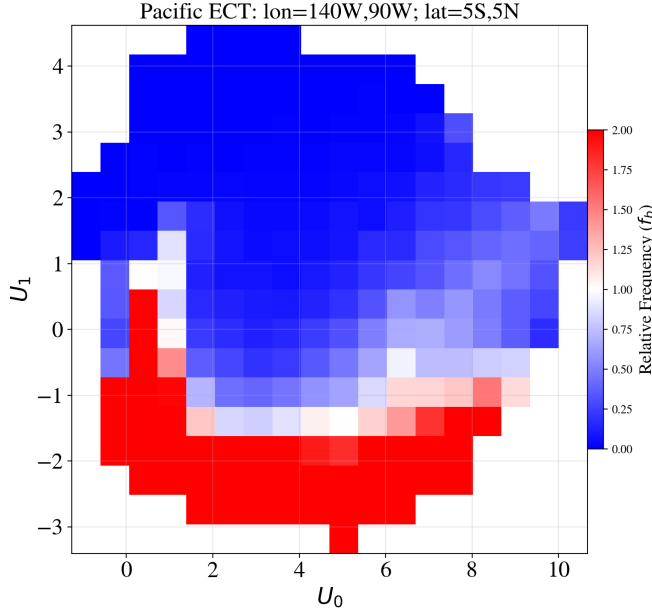


Fig. 13: Two-dimensional histogram of the relative frequency of specific SST patterns for $\Delta T = 0.5 - 1$ K in the Pacific ECT. This region is identified by the dashed black rectangle in Fig. 11 and contains 81,675 cutouts. The Pacific region is dominated by patterns with temperature variance at large scales (low U_1 and low U_0) and patterns with blemishes suggestive of unmasked clouds (low U_1 and high U_0). Bins with fewer than 200 cutouts have been excluded from the panels.

from the ≈ 2 km sampling of the data to the full extent of the cutouts. Furthermore, NENYA separates patterns with predominantly linear structures from those with significant curvature. In essence, NENYA defines a vocabulary for the language of SST imagery at the sub-mesoscale.

Leveraging this vocabulary, we examined the preferred geographical distribution of several sets of SST patterns. NENYA reveals that SST patches with temperature variance on scales larger than the sub-mesoscale occur preferentially in several distinct and large regions at low latitudes. These include the Pacific and Atlantic ECTs where the westward propagation of cool waters upwelled from eastern areas in the basin yield large temperature gradients along the equator. Additionally, we find that complex SST patterns with significant temperature variance on scales ranging from a few to tens of kilometers arise predominantly in dynamically active regions (e.g., western boundary currents) at high latitudes. These results confirm the direct mapping from SST patterns to distinct ocean processes.

Another application of NENYA is to resolve the principal SST patterns in select geographical regions. We recover highly distinct distributions of SST patterns when comparing the Pacific ECT (temperature variations primarily on large scales), a portion of the Gulf Stream near New England (complex SST patterns with temperature variance at a range of scales), and

the Equatorial Indian Ocean (primarily small-scale temperature variations). The distributions of these SST patterns are a fingerprint that define the regions and the dominant near-surface processes in these regions.

Last, we performed a time-series analysis of the defining patterns of the Pacific ECT and the Gulf Stream near New England to search for inter-annual and seasonal trends. We identify seasonal trends for each: the strengthening of the ECT in mid-summer months and the depression of dynamic features in/near the Gulf Stream during the summer.

We conclude, at least statistically, that a vocabulary that defines SST patterns provides a novel approach to tracking physical processes across the global ocean and dissecting such processes within distinct regions. Emboldened by this success, we will regress these patterns, specifically the full latent space representation of NENYA, against specific dynamic processes (e.g., frontogenesis) to leverage SST as an indirect descriptor of such dynamics. This will require performing analysis and training on ocean model output with known dynamics, e.g., the LLC4320 ocean general circulation model [39]–[41]. Ultimately, we may track the roles of sub-mesoscale processes in mixing and energy dissipation across the globe over the past two decades.

With this publication, we provide all of the data, outputs, and software related to NENYA and this manuscript. We also provide on-line visualization tools that enable the community to explore SST patterns from the dataset and those provided by the user. See XXX for full details.

TABLE I: MODIS Cutouts

| lon (deg) | lat (deg) | date | ΔT (K) | α_{\min} | LL | $U_{0,\text{all}}$ | $U_{1,\text{all}}$ | U_0 | U_1 |
|--------------|--------------|---------------------|-------------------|-----------------|-------|--------------------|--------------------|-------|-------|
| 8.688 | -32.425 | 2003-01-01 00:35:00 | 0.495 | -1.86 | 172.7 | 3.9 | 3.5 | -1.6 | 5.3 |
| 9.434 | -33.705 | 2003-01-01 00:35:00 | 0.655 | -1.77 | 204.6 | 0.1 | 2.7 | 6.8 | 2.2 |
| 10.311 | -33.231 | 2003-01-01 00:35:00 | 0.689 | -1.83 | 90.3 | 1.8 | 2.0 | 9.1 | 1.6 |
| 8.381 | -33.559 | 2003-01-01 00:35:00 | 0.712 | -2.18 | 188.9 | -0.3 | 3.6 | 7.4 | 0.9 |
| 9.303 | -32.807 | 2003-01-01 00:35:00 | 0.754 | -1.85 | 137.0 | 2.0 | 1.2 | 9.0 | 1.2 |
| 9.151 | -33.372 | 2003-01-01 00:35:00 | 0.536 | -1.68 | 212.0 | -0.7 | 2.6 | 8.0 | 0.9 |
| 11.091 | -33.327 | 2003-01-01 00:35:00 | 0.470 | -1.87 | 274.6 | 2.7 | 2.2 | -0.0 | 0.8 |
| 10.385 | -32.951 | 2003-01-01 00:35:00 | 0.605 | -1.77 | 149.0 | 2.4 | 2.0 | 8.9 | 0.2 |
| 11.023 | -33.612 | 2003-01-01 00:35:00 | 0.374 | -1.93 | 312.6 | 3.3 | 3.6 | -0.4 | 1.1 |
| 9.030 | -32.474 | 2003-01-01 00:35:00 | 0.645 | -1.78 | 183.6 | 1.0 | 2.1 | 8.1 | 1.6 |
| 9.940 | -33.183 | 2003-01-01 00:35:00 | 0.679 | -1.95 | 110.6 | 1.5 | 3.3 | 9.2 | 1.5 |
| 9.176 | -31.906 | 2003-01-01 00:35:00 | 0.415 | -2.05 | 242.9 | 2.3 | 3.1 | 0.3 | 4.3 |
| 9.506 | -33.420 | 2003-01-01 00:35:00 | 0.707 | -1.63 | 187.1 | 0.3 | 2.8 | 8.3 | 1.0 |
| 9.869 | -33.468 | 2003-01-01 00:35:00 | 0.715 | -2.07 | 108.1 | 0.8 | 1.9 | 8.9 | 1.9 |
| 8.613 | -32.710 | 2003-01-01 00:35:00 | 0.518 | -1.83 | 161.0 | 3.7 | 3.7 | 9.4 | 0.8 |
| 8.348 | -32.376 | 2003-01-01 00:35:00 | 0.418 | -1.86 | 162.4 | 4.4 | 3.9 | -2.0 | 5.3 |
| 10.016 | -32.903 | 2003-01-01 00:35:00 | 0.565 | -1.82 | 152.3 | 2.6 | 3.7 | 8.9 | 0.6 |
| 10.241 | -33.515 | 2003-01-01 00:35:00 | 0.748 | -2.05 | 111.9 | 1.2 | 1.7 | 9.0 | 1.9 |
| 10.454 | -32.666 | 2003-01-01 00:35:00 | 0.412 | -1.67 | 249.4 | 3.8 | 3.1 | -0.6 | 4.6 |
| 11.876 | -33.711 | 2003-01-01 00:35:00 | 0.386 | -1.95 | 384.9 | 3.9 | 4.6 | 1.6 | 4.0 |
| 10.085 | -32.618 | 2003-01-01 00:35:00 | 0.420 | -1.69 | 250.1 | 3.8 | 3.5 | -0.4 | 4.4 |

Notes: The ΔT value listed here is measured from the inner 40×40 pixel² region of the cutout.

LL is the log-likelihood metric calculated from the ULMO algorithm.

$U_{0,\text{all}}, U_{1,\text{all}}$ are the UMAP values for the UMAP analysis on the full dataset.

U_0, U_1 are the UMAP values for the UMAP analysis in the ΔT bin for this cutout.

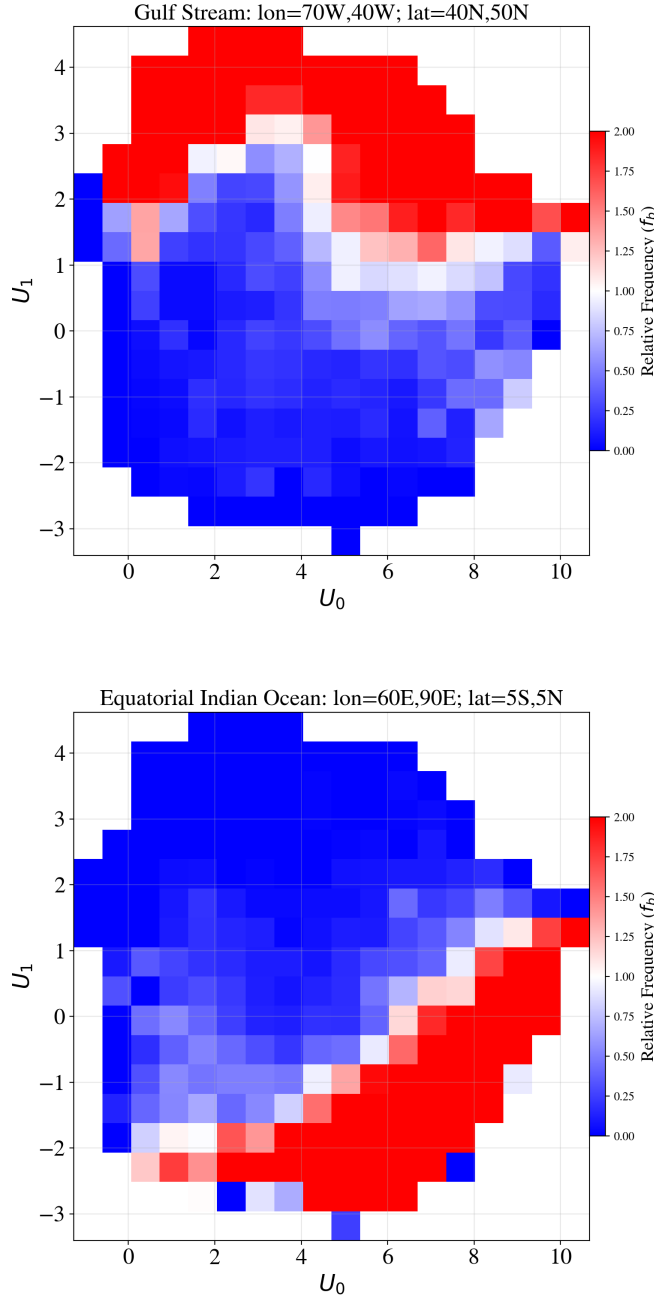


Fig. 14: Similar to Figure 13 but for SST patterns of the $\Delta T = 0.5 - 1$ K subset and for the Gulf Stream near New England (top) and the Equatorial Indian Ocean (bottom). The precise regions evaluated are labeled on the figures and shown in Figure 12 and each contains approximately 10,000 cutouts. The Gulf Stream shows an excess of patterns within the energetic region of the UMAP space (dashed ellipse in Figure 10) which have temperature variance at a wide range of scales. In contrast, the Equatorial Indian Ocean primarily exhibits patterns with small-scale variations, including those most similar to white noise (described by the dotted ellipse in Figure 10).

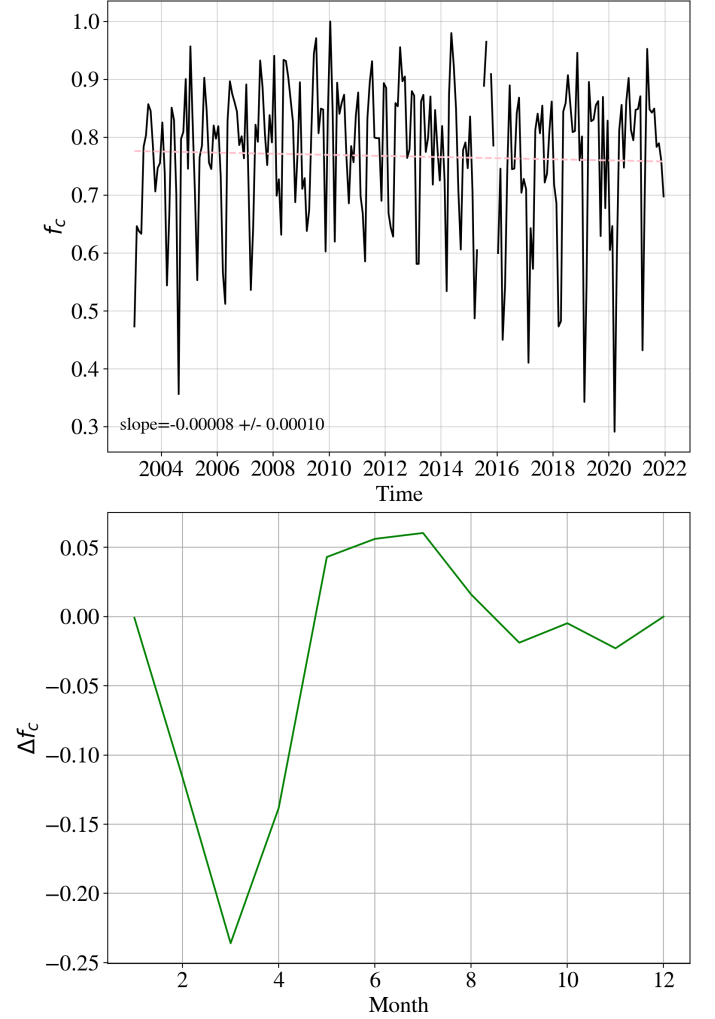


Fig. 15: Time series analysis of the cutout fraction for the prominent SST patterns of the Pacific ECT (limited to $\Delta T = 0.5 - 1$ K). These are defined by the portion of the UMAP domain where $f_b > 1.5$ in Figure 13. A cutout fraction $f_c=1$ indicates all of the cutouts in that month and year have these patterns. The upper panel shows the full time-series of f_c and the dashed line is a fit to the inter-annual trend accounting for seasonal variations. There is a strong seasonal signature (lower panel) associated with the intensification of the ECT by an increase in northward wind stress [23].

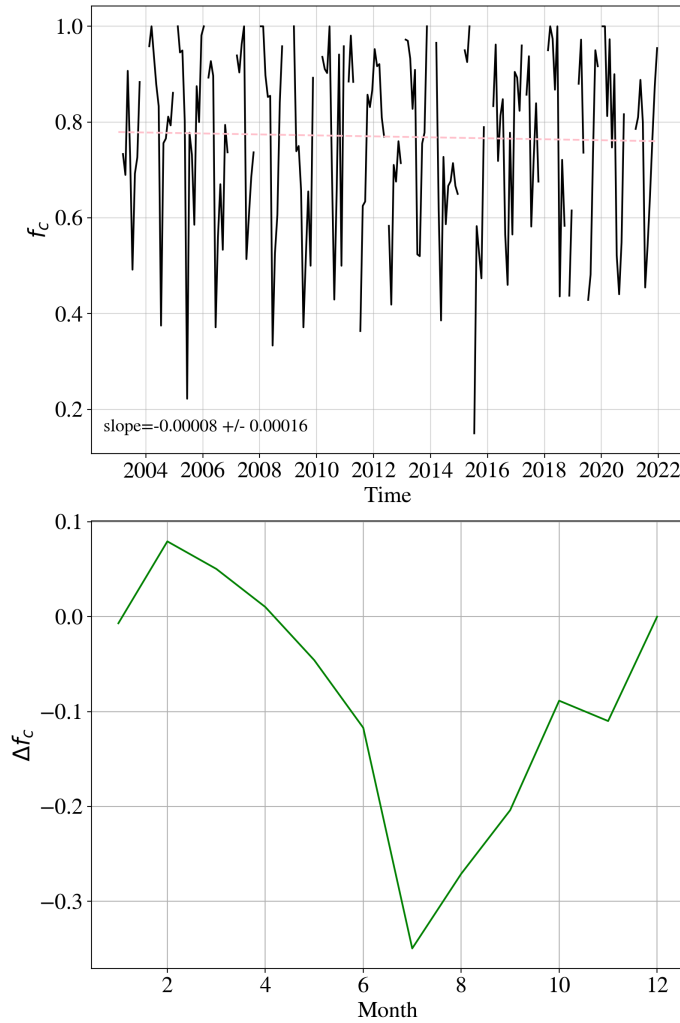


Fig. 16: Same as for Figure 15 but for the enhanced patterns of the Gulf Stream near New England, those with $f_b > 1.25$ in the upper panel of Figure 14. The incidence of these complex patterns exhibits a strong seasonal dependence, with a strong suppression during summer months possibly due to masking by the seasonal thermocline.

Acronyms

| | |
|----------------|--|
| ECT | equatorial cold tongue |
| HEALPix | Hierarchical Equal Area isoLatitude Pixelation |
| IR | infrared |
| L2 | Level-2 |
| LL | log-likelihood |
| ML | machine learning |
| MODIS | MODerate-resolution Imaging Spectroradiometer |
| PAE | probabilistic autoencoder |
| SSL | self-supervised learning |
| SST | sea surface temperature |
| SSTa | SST anomaly |
| UMAP | Uniform Manifold Approximation and Projection |

APPENDIX A ADDITIONAL GALLERIES

APPENDIX B

Appendix two text goes here.

ACKNOWLEDGMENT

JXP acknowledges future support from the Simons Foundation and help from Claudie Beaulieu for the time-series analysis. EG acknowledges J. Xavier Prochaska and P. C. Cornillon's invaluable guidance on this project, as well as David Draper's insightful discussions.

The authors acknowledge use of the Nautilus cloud computing system which is supported by the following US National Science Foundation (NSF) awards: CNS-1456638, CNS-1730158, CNS-2100237, CNS-2120019, ACI-1540112, ACI-1541349, OAC-1826967, OAC-2112167.

REFERENCES

- [1] L. N. Thomas, A. Tandon, and A. Mahadevan, "Submesoscale processes and dynamics," *Ocean Modeling in an Eddying Regime, Geophys. Monogr. Ser.*, vol. 177, pp. 17–38, 2008.
- [2] J. C. McWilliams, "Submesoscale currents in the ocean," *Proceedings of the Royal Society of London A: Mathematical, Physical and Engineering Sciences*, vol. 472, no. 2189, pp. 1–32, 2016.
- [3] J. X. Prochaska, P. C. Cornillon, and D. M. Reiman, "Deep learning of sea surface temperature patterns to identify ocean extremes," *Remote Sensing*, vol. 13, no. 4, 2021. [Online]. Available: <https://www.mdpi.com/2072-4292/13/4/744>
- [4] V. Böhm and U. Seljak, "Probabilistic auto-encoder," 2020.
- [5] R. Hadsell, S. Chopra, and Y. LeCun, "Dimensionality reduction by learning an invariant mapping," in *2006 IEEE Computer Society Conference on Computer Vision and Pattern Recognition (CVPR'06)*, vol. 2. IEEE, 2006, pp. 1735–1742.
- [6] P. Bachman, R. D. Hjelm, and W. Buchwalter, "Learning representations by maximizing mutual information across views," *arXiv preprint arXiv:1906.00910*, 2019.
- [7] T. Chen, S. Kornblith, M. Norouzi, and G. Hinton, "A simple framework for contrastive learning of visual representations," in *International conference on machine learning*. PMLR, 2020, pp. 1597–1607.
- [8] T. Chen, S. Kornblith, K. Swersky, M. Norouzi, and G. Hinton, "Big self-supervised models are strong semi-supervised learners," *arXiv preprint arXiv:2006.10029*, 2020.
- [9] X. Chen, H. Fan, R. Girshick, and K. He, "Improved baselines with momentum contrastive learning," *arXiv preprint arXiv:2003.04297*, 2020.
- [10] K. He, H. Fan, Y. Wu, S. Xie, and R. Girshick, "Momentum contrast for unsupervised visual representation learning," in *Proceedings of the IEEE/CVF Conference on Computer Vision and Pattern Recognition*, 2020, pp. 9729–9738.
- [11] Y. Tian, C. Sun, B. Poole, D. Krishnan, C. Schmid, and P. Isola, "What makes for good views for contrastive learning?" *arXiv preprint arXiv:2005.10243*, 2020.
- [12] M. A. Hayat, G. Stein, P. Harrington, Z. Lukić, and M. Mustafa, "Self-supervised Representation Learning for Astronomical Images," *The Astrophysical Journal Letters*, vol. 911, no. 2, p. L33, Apr. 2021.
- [13] W. Morningstar, C. Ham, A. G. Gallagher, B. Lakshminarayanan, A. A. Alemi, and J. V. Dillon, "Density of states estimation for out-of-distribution detection," in *AISTATS*, 2021.
- [14] J. Charney, "Geostrophic turbulence," *J. Atmos. Sci.*, vol. 28, pp. 1087–1095, 1971.
- [15] C. Garrett and W. Munk, "Space-time scales of internal waves," *Geophys. Fluid Dyn.*, vol. 3, pp. 225–264, 1972.
- [16] J. Callies and R. Ferrari, "Interpreting energy and tracer spectra of upper-ocean turbulence in the submesoscale range (1–200 km)," *Journal of Physical Oceanography*, vol. 43, pp. 2456–2474, 2013. [Online]. Available: <https://journals.ametsoc.org/view/journals/phoc/43/11/jpo-d-13-063.1.xml>
- [17] L. McInnes, J. Healy, and J. Melville, "UMAP: Uniform Manifold Approximation and Projection for Dimension Reduction," *ArXiv e-prints*, Feb. 2018.
- [18] S. Cheng and B. Ménard, "How to quantify fields or textures? A guide to the scattering transform," *arXiv e-prints*, p. arXiv:2112.01288, Nov. 2021.
- [19] S. Mallat, "Group invariant scattering," *Communications on Pure and Applied Mathematics*, vol. 65, no. 10, pp. 1331–1398, 2012. [Online]. Available: <https://onlinelibrary.wiley.com/doi/abs/10.1002/cpa.21413>
- [20] K. He, X. Zhang, S. Ren, and J. Sun, "Deep residual learning for image recognition," in *Proceedings of the IEEE conference on computer vision and pattern recognition*, 2016, pp. 770–778.
- [21] L. McInnes, J. Healy, N. Saul, and L. Großberger, "Umap: Uniform manifold approximation and projection," *Journal of Open Source Software*, vol. 3, no. 29, p. 861, 2018. [Online]. Available: <https://doi.org/10.21105/joss.00861>
- [22] K. M. Górski, E. Hivon, A. J. Banday, B. D. Wandelt, F. K. Hansen, M. Reinecke, and M. Bartelmann, "HEALPix: A Framework for High-Resolution Discretization and Fast Analysis of Data Distributed on the Sphere," *The Astrophysical Journal*, vol. 622, no. 2, pp. 759–771, Apr. 2005.
- [23] T. P. Mitchell and J. M. Wallace, "The annual cycle in equatorial convection and sea surface temperature," *Journal of Climate*, vol. 5, no. 10, pp. 1140 – 1156, 1992. [Online]. Available: https://journals.ametsoc.org/view/journals/clim/5/10/1520-0442_1992_005_1140_taciec_2_0_co_2.xml
- [24] Y. Okumura and S.-P. Xie, "Interaction of the atlantic equatorial cold tongue and the african monsoon," *Journal of Climate*, vol. 17, no. 18, pp. 3589–3602, 2004.
- [25] J. Pedlosky, *Geophysical Fluid Dynamics*, 2nd ed. New York, NY, USA: Springer-Verlag, 1990.
- [26] E. Hagen, "Zonal wavelengths of planetary rossby waves derived from hydrographic transects in the northeast atlantic ocean?" *J. Oceanography*, vol. 61, pp. 1039–1046, 2005.
- [27] L. Kounta, X. Capet, J. Jouanno, N. Kolodziejczyk, B. Sow, and A. T. Gaye, "A model perspective on the dynamics of the shadow zone of the eastern tropical north atlantic – part 1: the poleward slope currents along west africa," *Ocean Science*, vol. 14, no. 5, pp. 971–997, 2018. [Online]. Available: <https://os.copernicus.org/articles/14/971/2018/>
- [28] C. S. Willett, R. R. Leben, and M. F. Lavín, "Eddies and tropical instability waves in the eastern tropical pacific: A review," *Progress in Oceanography*, vol. 69, no. 2, pp. 218–238, 2006, a Review of Eastern Tropical Pacific Oceanography. [Online]. Available: <https://www.sciencedirect.com/science/article/pii/S0079661106000322>
- [29] L. Stramma, S. Hüttel, and J. Schafstall, "Water masses and currents in the upper tropical northeast atlantic off northwest africa," *Journal of Geophysical Research: Oceans*, vol. 110, no. C12, 2005. [Online]. Available: <https://agupubs.onlinelibrary.wiley.com/doi/abs/10.1029/2005JC002939>
- [30] V. Combes and R. P. Matano, "The patagonian shelf circulation: Drivers and variability," *Progress in Oceanography*, vol. 167, pp. 24–43, 2018. [Online]. Available: <https://www.sciencedirect.com/science/article/pii/S0079661117303130>
- [31] S. C. Painter, "The biogeochemistry and oceanography of the east african coastal current," *Progress in Oceanography*, vol. 186, p. 102374, 2020. [Online]. Available: <https://www.sciencedirect.com/science/article/pii/S0079661120301130>
- [32] D. B. Chelton, M. G. Schlax, and R. M. Samelson, "Global observations of nonlinear mesoscale eddies," *Progress in Oceanography*, vol. 91, no. 2, pp. 167 – 216, 2011. [Online]. Available: <http://www.sciencedirect.com/science/article/pii/S0079661111000036>
- [33] A. Chatterjee, D. Shankar, J. McCreary, P. Vinayachandran, and A. Mukherjee, "Dynamics of andaman sea circulation and its role in connecting the equatorial indian ocean to the bay of bengal," *Journal of Geophysical Research: Oceans*, vol. 122, no. 4, pp. 3200–3218, 2017.
- [34] A. Huyer, "Coastal upwelling in the california current system," *Progress in oceanography*, vol. 12, no. 3, pp. 259–284, 1983.
- [35] Y. Freund and M. L., "The alternating decision tree learning algorithm," in *Proceedings of the 16th International Conference on Machine Learning*. San Francisco, CA, USA: Morgan Kaufmann Publishers Inc., 1999, pp. 124–133.
- [36] Y. Tanaka and T. Hibiya, "Generation mechanism of tropical instability waves in the equatorial pacific ocean," *Journal of Physical Oceanography*, vol. 49, no. 11, pp. 2901 – 2915, 2019. [Online]. Available: <https://journals.ametsoc.org/view/journals/phoc/49/11/jpo-d-19-0094.1.xml>
- [37] D. B. Chelton, S. K. Esbensen, M. G. S. and Nicolai Thum, M. H. Freilich, F. J. Wentz, C. L. G. nn, M. J. McPhaden, and P. S. Schopf, "Observations of coupling between surface wind stress and sea surface temperature in the eastern tropical pacific,"

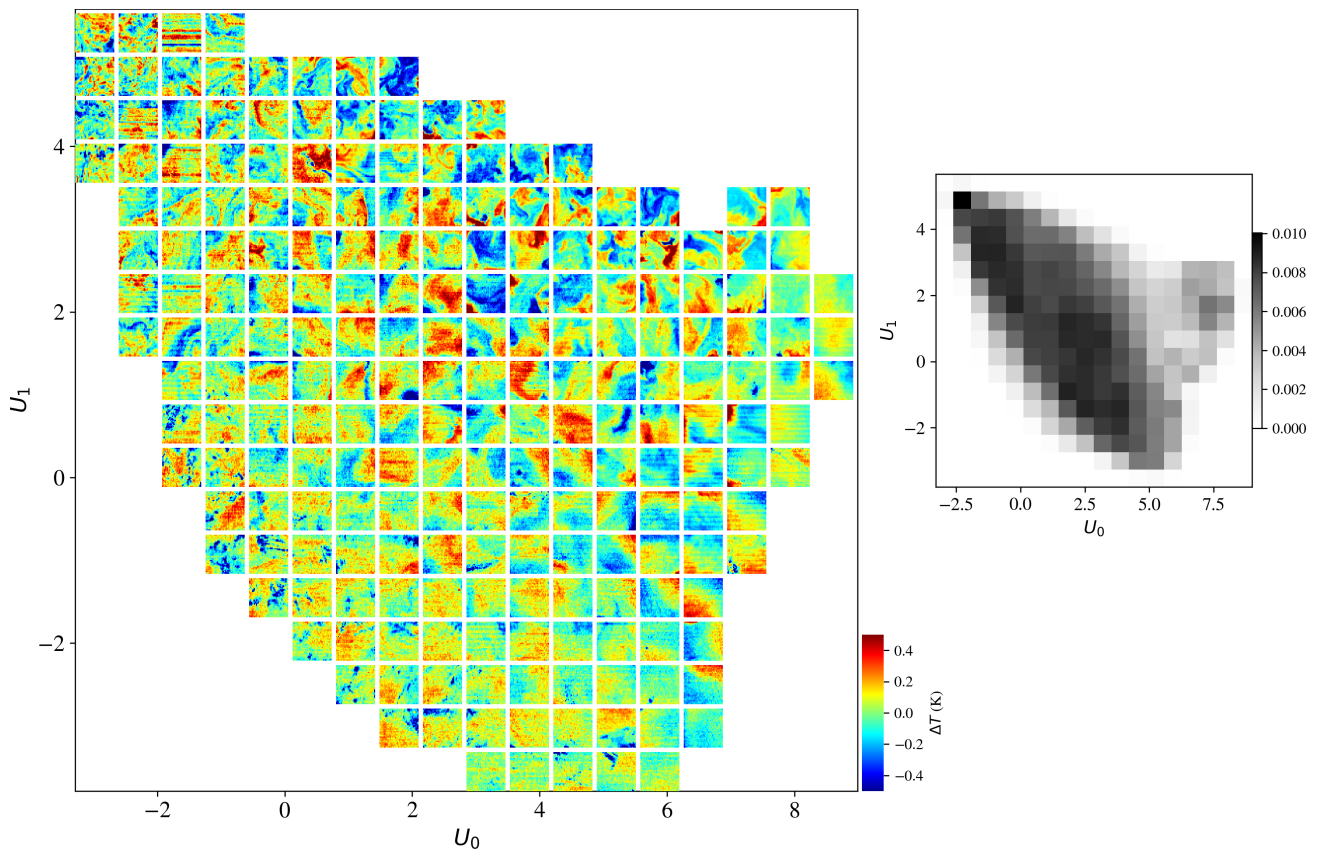


Fig. 17: Same as Figure 7 but for the UMAP embedding of the $\Delta T = 0 - 0.5$ K sub-set of cutouts.

Journal of Climate, vol. 14, no. 7, pp. 1479 – 1498, 2001.
[Online]. Available: https://journals.ametsoc.org/view/journals/clim/14/7/1520-0442_2001_014_1479_oocbsw_2.0.co_2.xml

- [38] S. Ray, A. T. Wittenberg, S. M. Griffies, and F. Zeng, “Understanding the equatorial pacific cold tongue time-mean heat budget. part i: Diagnostic framework,” *Journal of Climate*, vol. 31, no. 24, pp. 9965 – 9985, 2018. [Online]. Available: <https://journals.ametsoc.org/view/journals/clim/31/24/jcli-d-18-0152.1.xml>
- [39] C. B. Rocha, T. K. Chereskin, S. T. Gille, and D. Menemenlis, “Mesoscale to Submesoscale Wavenumber Spectra in Drake Passage,” *Journal of Physical Oceanography*, vol. 46, no. 2, pp. 601–620, feb 2016.
- [40] C. B. Rocha, S. T. Gille, T. K. Chereskin, and D. Menemenlis, “Seasonality of submesoscale dynamics in the Kuroshio Extension,” *Geophysical Research Letters*, vol. 43, no. 21, pp. 11 304–11 311, nov 2016.
- [41] B. K. Arbic, M. H. Alford, J. K. Ansong, M. C. Buijsman, R. B. Ciotti, J. T. Farrar, R. W. Hallberg, C. E. Henze, C. N. Hill, C. A. Luecke, D. Menemenlis, E. J. Metzger, M. Müller, A. D. Nelson, B. C. Nelson, H. E. Ngodock, R. M. Ponte, J. G. Richman, A. C. Savage, R. B. Scott, J. F. Shriver, H. L. Simmons, I. Souopgui, P. G. Timko, A. J. Wallcraft, L. Zamudio, and Z. Zhao, “A Primer on Global Internal Tide and Internal Gravity Wave Continuum Modeling in HYCOM and MITgcm,” in *New Frontiers in Operational Oceanography*, E. P. Chassignet, A. Pascual, J. Tintoré, and J. Verron, Eds. GODAE OceanView, aug 2018, ch. 13, pp. 307–392.

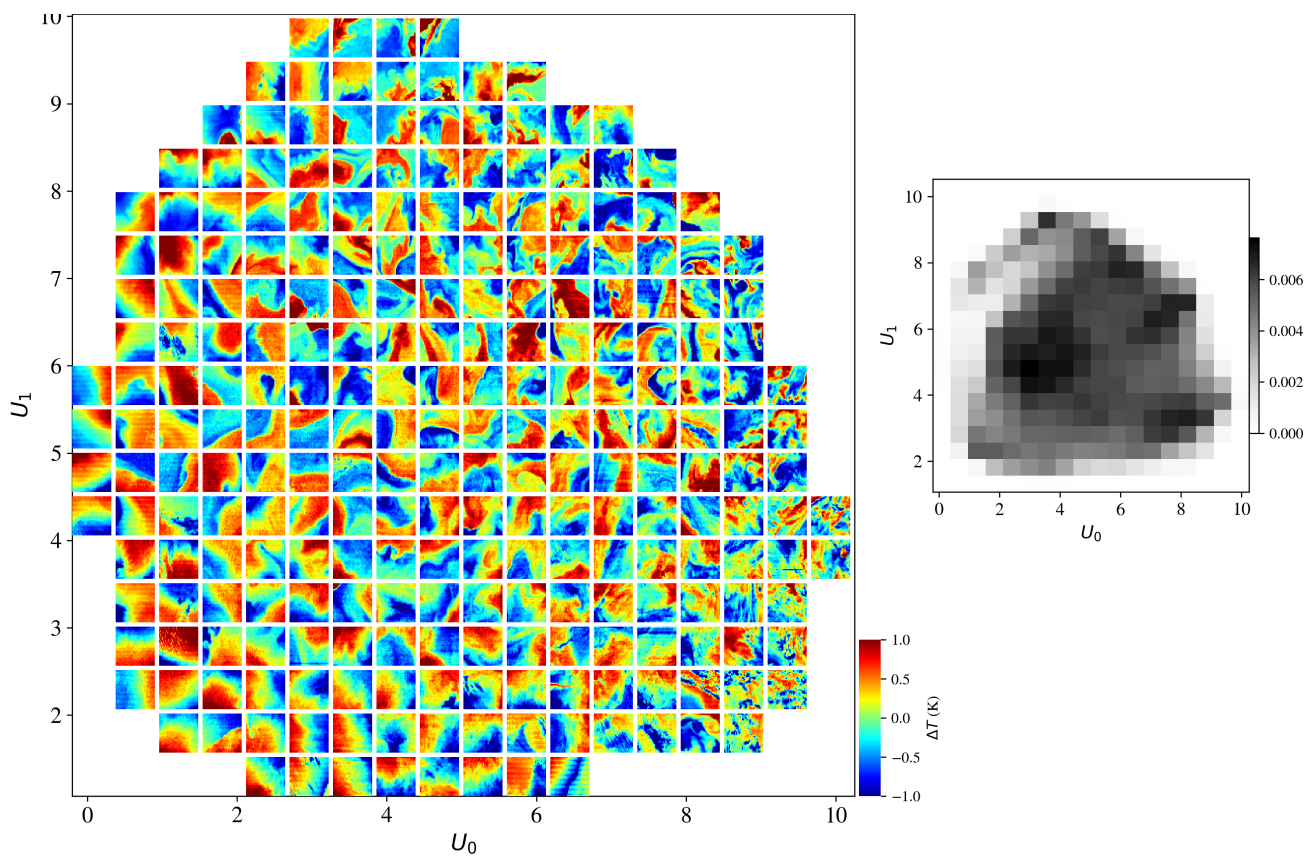


Fig. 18: Same as Figure 7 but for the UMAP embedding of the $\Delta T = 1 - 1.5$ K sub-set of cutouts.

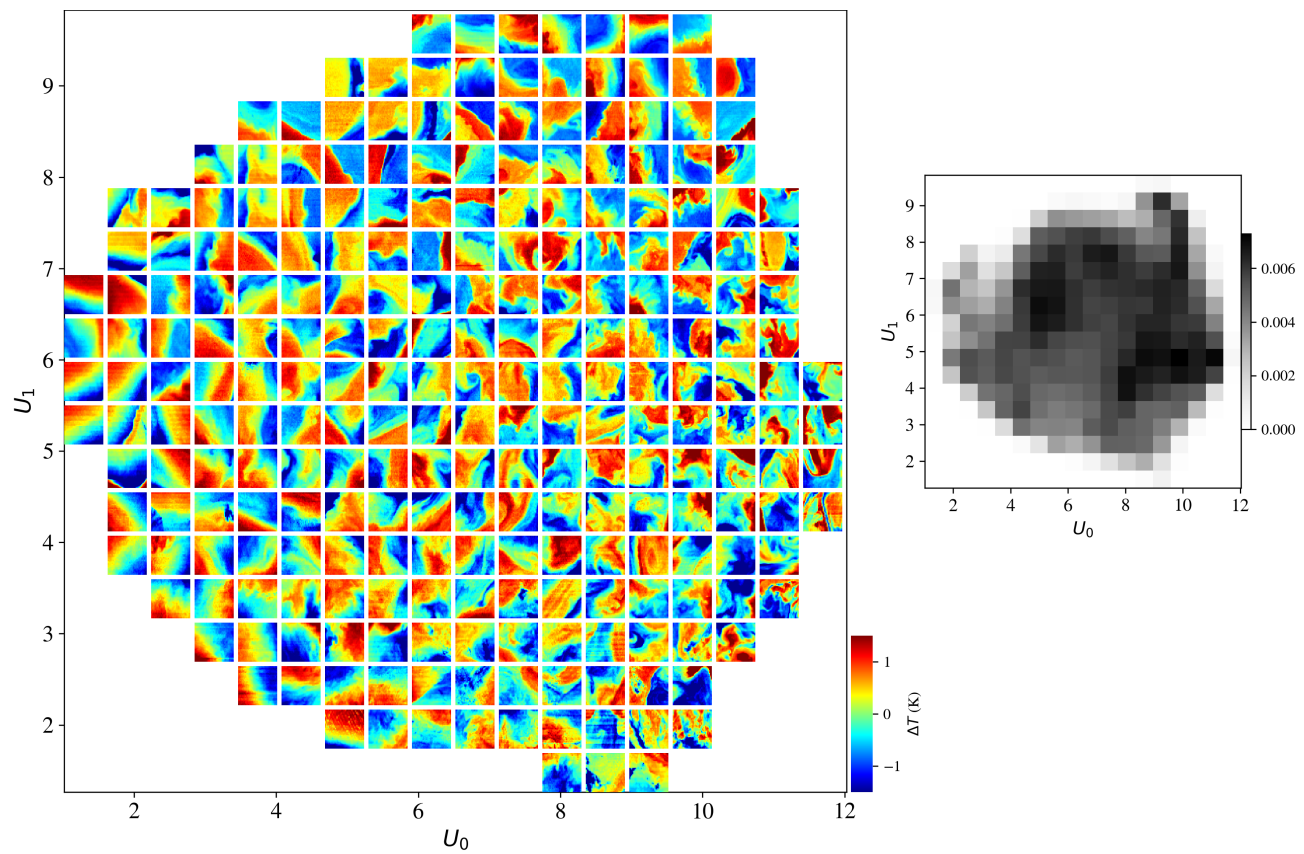


Fig. 19: Same as Figure 7 but for the UMAP embedding of the $\Delta T = 1.5 - 2.5$ K sub-set of cutouts.

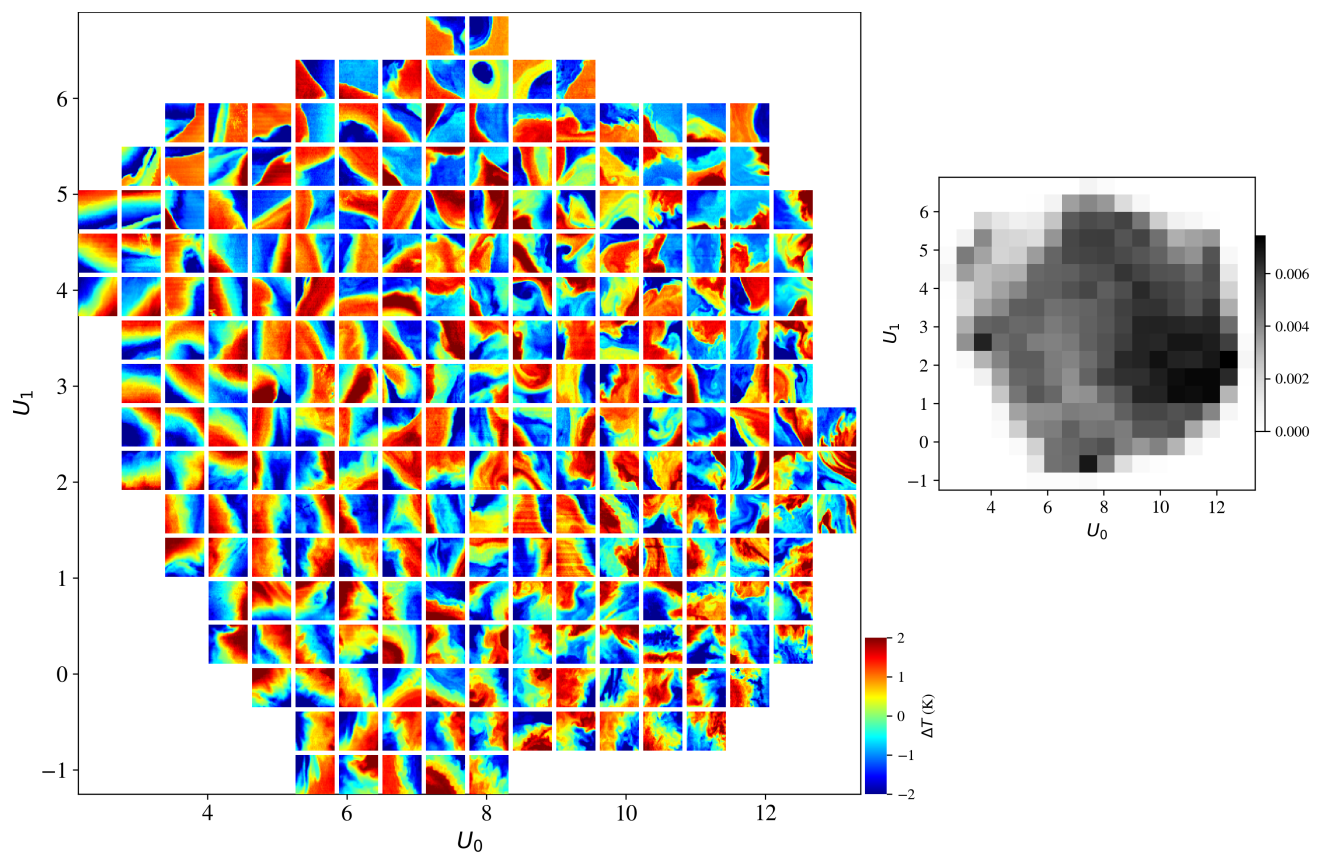


Fig. 20: Same as Figure 7 but for the UMAP embedding of the $\Delta T = 2.5 - 4$ K sub-set of cutouts.

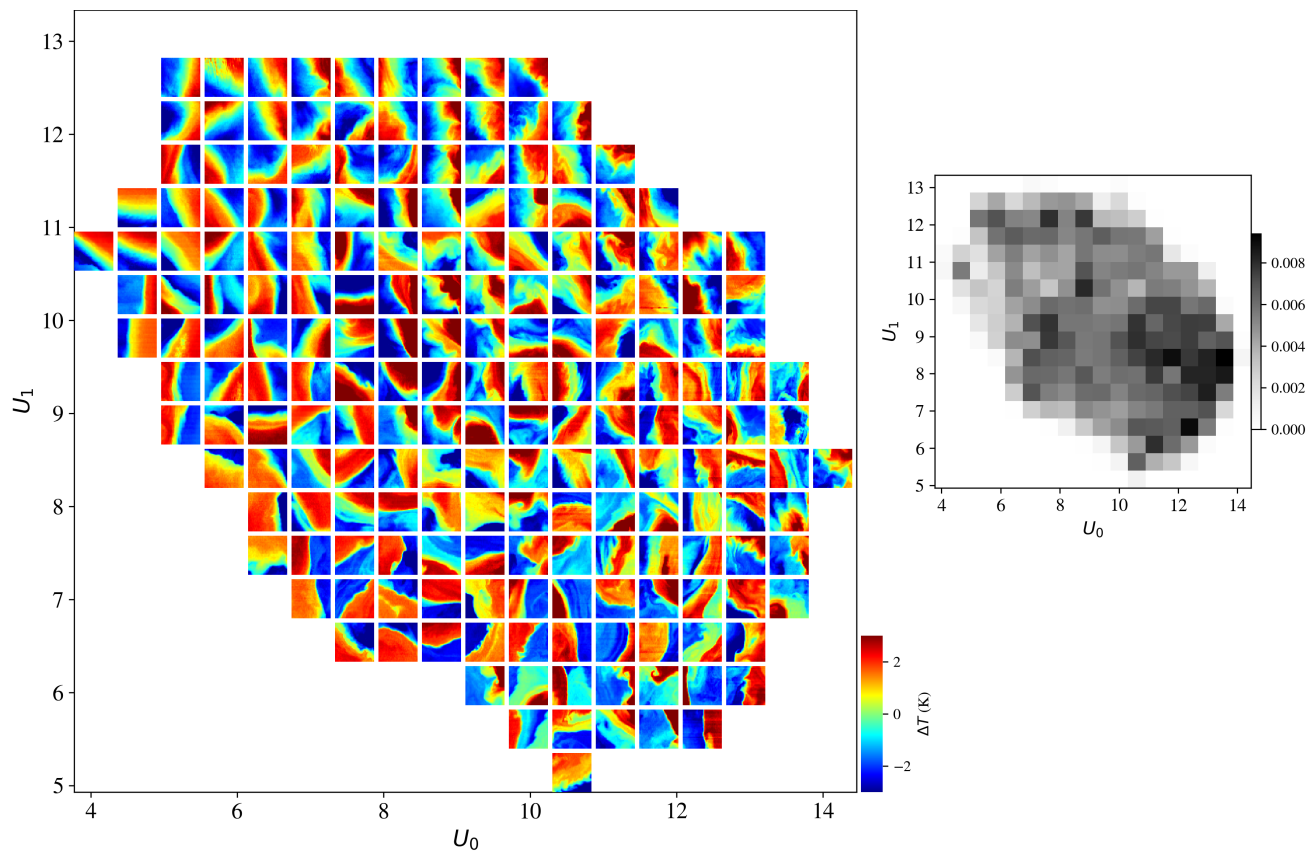


Fig. 21: Same as Figure 7 but for the UMAP embedding of the $\Delta T > 4$ K sub-set of cutouts.